

# Spatiotemporal Pyramid Flow Matching for Climate Emulation

Jeremy A. Irvin<sup>1\*</sup>, Jiaqi Han<sup>1</sup>, Zikui Wang<sup>1</sup>, Abdulaziz Alharbi<sup>1</sup>, Yufei Zhao<sup>1</sup>,  
Nomin-Erdene Bayarsaikhan<sup>1</sup>, Daniele Visoni<sup>2</sup>, Andrew Y. Ng<sup>1</sup>, Duncan Watson-Parris<sup>3</sup>

<sup>1</sup>Stanford University

<sup>2</sup>Cornell University

<sup>3</sup>University of California, San Diego

## Abstract

*Generative models have the potential to transform the way we emulate Earth’s changing climate. Previous generative approaches rely on weather-scale autoregression for climate emulation, but this is inherently slow for long climate horizons and has yet to demonstrate stable rollouts under nonstationary forcings. Here, we introduce Spatiotemporal Pyramid Flows (SPF), a new class of flow matching approaches that model data hierarchically across spatial and temporal scales. Inspired by cascaded video models, SPF partitions the generative trajectory into a spatiotemporal pyramid, progressively increasing spatial resolution to reduce computation and coupling each stage with an associated timescale to enable direct sampling at any temporal level in the pyramid. This design, together with conditioning each stage on prescribed physical forcings (e.g., greenhouse gases or aerosols), enables efficient, parallel climate emulation at multiple timescales. On ClimateBench, SPF outperforms strong flow matching baselines and pre-trained models at yearly and monthly timescales while offering fast sampling, especially at coarser temporal levels. To scale SPF, we curate ClimateSuite, the largest collection of Earth system simulations to date, comprising over 33,000 simulation-years across ten climate models and the first dataset to include simulations of climate interventions. We find that the scaled SPF model demonstrates good generalization to held-out scenarios across climate models. Together, SPF and ClimateSuite provide a foundation for accurate, efficient, probabilistic climate emulation across temporal scales and realistic future scenarios. Data and code is publicly available at [github.com/stanfordmlgroup/spf](https://github.com/stanfordmlgroup/spf).*

## 1. Introduction

Climate models (Earth system models; ESMs) are the primary scientific instruments for quantifying how the Earth’s climate will evolve under changing emissions and interventions. They resolve interacting physical processes across a

wide range of spatial and temporal scales, but this fidelity comes with enormous computational cost: long rollouts (decades to centuries), ensembles for uncertainty quantification, and large design sweeps across forcings make systematic exploration prohibitive even on state-of-the-art supercomputers [14, 16, 26]. As a consequence, scientists and policymakers are constrained to a narrow set of scenarios and limited ensemble sizes, which hinders robust assessment of regional risks and of policy-relevant choices such as emissions pathways or climate interventions [30, 40, 54]. These pressures have led to increasing interest in data-driven surrogates that efficiently emulate ESMs while remaining accurate, stable, and physically plausible over very long horizons [5, 54, 56].

Recent work has made tangible progress toward this goal, but it has relied primarily on autoregressive emulation at the weather-scale (short term) rolled out over climate-scale (long term) periods [5, 28, 56, 57]. This approach inherits two central limitations for climate emulation: first, weather-scale autoregressive models are subject to small local errors that compound over time, leading to drift in long-term statistics. Although recent models have demonstrated decade-long rollouts with small climatological biases in a simplified atmospheric model with fixed forcings, they have yet to capture realistic climate trends driven by greenhouse gas emissions or aerosols [56, 57]. Second, long-horizon rollouts remain computationally expensive due to the large number of sequential autoregressive steps; for example, generating a single 10-year trajectory with a state-of-the-art emulator takes nearly three hours [5]. This is especially prohibitive for many practical downstream uses which only require coarser timescale samples, e.g., annual indicators for integrated assessment models and policy assessments, or monthly fields for sectoral impact studies [15, 51]. In parallel, regression-based emulators that directly map external forcings to long-term mean climate responses offer an alternative path toward efficiency [39, 54]. Our approach builds upon regression-based methods to capture multiple timescales within a single model and support parallel sampling of temporal sequences, leading to additional efficiency gains for long time horizons.

\*Correspondence to: [jirvin16@cs.stanford.edu](mailto:jirvin16@cs.stanford.edu)

Beyond accuracy and efficiency, a critical requirement for climate emulation is the ability to represent uncertainty. In Earth system modeling, ensembles of simulations are used to quantify variability and assess the likelihood of climate outcomes. Similarly, probabilistic emulators should generate diverse samples from a learned distribution, allowing estimation of uncertainty and exploration of alternative trajectories under the same forcing conditions. Only recently has work begun to address this need by developing stochastic climate-scale emulators capable of sampling multiple plausible futures [3, 5, 28].

Diffusion and flow-based image and video generative models offer a promising path toward emulators that combine efficiency with probabilistic generation. These models provide a flexible framework for sampling from complex multimodal data distributions and have demonstrated remarkable success on image [20, 32] and video generation tasks [23, 24]. However, most high-quality video models (i) rely on autoregression through time to model long sequences, which scales poorly [7] and/or (ii) compress the high-dimensional spatiotemporal data into low-dimensional latents using a strong variational autoencoder (VAE), a component that is unavailable for climate data, difficult to train, and constrains performance to the quality of the learned compression [17, 24, 29, 33, 43]. We address these challenges with an efficient parallel approach operating in pixel space, eliminating the need for a separate VAE.

A key algorithmic insight from the natural image and video domains is to cascade generation: model coarse structure first and then refine in multiple stages, thereby concentrating compute where it most affects perceptual quality [22]. Recent work performs this cascade within a single model by partitioning the flow into stages at different spatial resolutions, yielding faster sampling and a lower memory footprint than a full-resolution flow while allowing knowledge sharing between stages [8, 24]. For climate data, an analogous inductive bias exists in both space and time. Spatially, large scales organize small scales through energy and moisture transports; temporally, slow components such as forced trends and interannual variability modulate fast weather fluctuations. Rather than explicitly modeling these long-term dependencies through extended rollouts, conditioning the model on physical forcings (e.g., greenhouse gases, aerosols, or solar variability) allows the emulator to capture slow, externally driven trends without requiring access to long historical sequences, as framed in Watson-Parris et al. [54]. This provides a principled path to long-horizon efficiency: learn flows that represent coarse, slow components in latent space and progressively refine them across scales to circumvent fine-step autoregression.

In this work, we introduce **Spatiotemporal Pyramid Flows (SPF)**, a class of flow matching models that generalize pyramid flows for efficient emulation across timescales.

SPF partitions the generative trajectory into a spatiotemporal pyramid that (i) models coarse-resolution, long-horizon climate states that encode externally forced trends and low-frequency variability, (ii) conditionally refines spatial detail, and (iii) conditionally refines temporal resolution, enabling direct sampling at arbitrary future times without rolling forward step by step. By conditioning each stage on prescribed physical forcings, SPF can funnel into specific spatial or temporal windows while maintaining long-term physical coherence. Crucially, this formulation generalizes prior pyramid flow methods by allowing arbitrary resampling between stages and by supporting clean generation from any level of the hierarchy, yielding efficient sampling across timescales relevant for climate-scale downstream tasks.

To train a scaled SPF model, we curate **ClimateSuite**, the largest ML-ready climate modeling dataset to date with more than 33,000 simulation-years of data from 10 ESMs. As climate emulators are increasingly expected to support policy-relevant questions, such as responses to climate interventions, we include 39 stratospheric aerosol injection (SAI) experiments in addition to 276 non-SAI experiments. We publicly release ClimateSuite to facilitate the development of strong and efficient climate emulators across different ESMs, emissions scenarios, and interventions.

Altogether, our contributions are as follows:

1. We introduce a new class of flow matching approaches called Spatiotemporal Pyramid Flows (SPF) that enable efficient and accurate sampling by applying a pyramid of resolution-cascaded flows across both space and time. SPF refines noised latent trajectories conditioned on physical forcings, enabling accurate sampling of emulated climate model outputs at arbitrary future times without autoregressive simulation.
2. We show that SPF generalizes prior pyramid flow approaches [8, 24], importantly supporting arbitrary resolution resampling between stages and enabling generation of clean samples from any timescale in the pyramid.
3. We curate and publicly release the largest dataset for climate model emulation to date, ClimateSuite, comprising more than 33,000 simulation-years of climate data spanning 276 state-of-the-art simulations from 10 ESMs and 39 SAI simulations. This substantially expands the data available for developing ML-based climate emulators.
4. We demonstrate that SPF achieves superior accuracy and inference efficiency compared to strong deterministic baselines, pre-trained models, and flow matching approaches on ClimateBench [54]. Training SPF on ClimateSuite leads to good generalization to emissions and intervention scenarios across climate models, and improves performance on ClimateBench after fine-tuning.



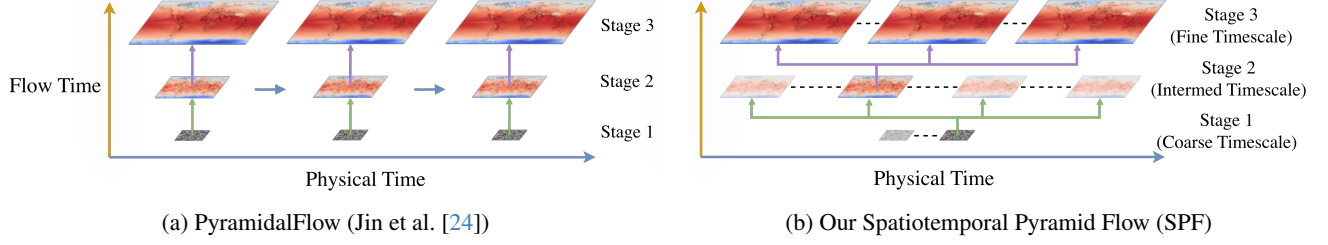


Figure 1. **Comparison between PyramidalFlow and our proposed approach.** (a) PyramidalFlow generates autoregressively, running one pyramid flow for every physical timestep. (b) Our method generates in parallel, running a joint flow to sample multiple timesteps at once. To save compute for long sequences, SPF can funnel into a chosen timestep before transitioning to the next timescale. Since timescale lengths differ (e.g. 10 years for decadal or 12 months for annual), SPF supports variable temporal (and spatial) transitions between stages.

## 2. Methods

### 2.1. Background

#### 2.1.1. Diffusion and Flow Matching

Diffusion models [20, 47, 48] and flow generative models [32, 34, 41, 42, 58] transform random noise  $\mathbf{x}_0 \sim \mathcal{N}(\mathbf{0}, \mathbf{I})$  into samples from a target data distribution  $\mathbf{x}_1 \sim q$  by learning a velocity field  $\mathbf{v}_t$  which prescribes an ordinary differential equation (ODE):

$$\frac{d\mathbf{x}_t}{dt} = \mathbf{v}_t(\mathbf{x}_t).$$

The velocity field is commonly learned using conditional flow matching, a simple simulation-free training objective to directly regress the velocity  $\mathbf{v}_t$  with a conditional (per-sample) vector field  $\mathbf{u}_t(\cdot|\mathbf{x}_1)$ :

$$\mathbb{E}_{t \sim \mathcal{U}[0,1], q(\mathbf{x}_1), p_t(\mathbf{x}_t|\mathbf{x}_1)} \|\mathbf{v}_t(\mathbf{x}_t) - \mathbf{u}_t(\mathbf{x}_t|\mathbf{x}_1)\|^2.$$

This is a tractable objective with the same optima as the marginal flow matching objective where the choice of  $\mathbf{u}_t(\cdot|\mathbf{x}_1)$  uniquely determines a conditional probability path  $p_t(\mathbf{x}_t|\mathbf{x}_1)$ , a time-dependent probability density function that describes how samples from the prior transform to samples from the target distribution.

A common and effective choice of vector field is  $\mathbf{u}(\mathbf{x}_t|\mathbf{x}_1) = \mathbf{x}_1 - \mathbf{x}_0$ , which induces a conditional probability path that linearly interpolates between noise and data:

$$\begin{aligned} \mathbf{x}_t &= t\mathbf{x}_1 + (1-t)\mathbf{x}_0 \\ \mathbf{x}_t &\sim \mathcal{N}(t\mathbf{x}_1, (1-t)^2\mathbf{I}). \end{aligned}$$

#### 2.1.2. Piecewise Flows

Piecewise flows [58] partition the flow trajectory into  $K$  segments  $\{[s_k, e_k]\}_{k=0}^{K-1}$  where  $0 = s_{K-1} < e_{K-1} = s_{K-2} < \dots < e_1 = s_0 < e_0 = 1$ . Each segment is endowed with its own probability path  $p_t^{(k)}$  and therefore its own target vector field  $\mathbf{u}_t^{(k)}(\mathbf{x}_t^{(k)})$ .

At inference time, the learned ODE on each segment is integrated in sequence, ensuring that the endpoints of each segment aligns (in distribution) with the endpoints of adjacent segments when necessary.

#### 2.1.3. Pyramid Flows

To reduce the computational cost of sampling images and videos, previous work has proposed constructing piecewise flows segmented by spatial resolution so only the final stage operates at the highest resolution [8, 24]. This design forms a spatial pyramid partitioned into  $K$  stages, where stage  $k$  denoises an image at lower spatial resolution which is subsequently upsampled and input to stage  $k-1$ , gradually denoising and increasing spatial resolution through the flow.

Formally, the flow within the  $k$ -th time window  $[s_k, e_k]$  is:

$$\mathbf{x}_t = t' \text{Down}(\mathbf{x}_{e_k}, 2^k) + (1-t') \text{Up}(\text{Down}(\mathbf{x}_{s_k}, 2^{k+1})),$$

where  $t' = (t - s_k)/(e_k - s_k)$  is the rescaled timestep, Down is a well-defined downsampling function (e.g., bilinear interpolation), and Up is an upsampling function (e.g., nearest neighbor interpolation). The conditional probability path is defined by:

$$\text{End: } \hat{\mathbf{x}}_{e_k} | \mathbf{x}_1 \sim \mathcal{N}(e_k \text{Down}(\mathbf{x}_1, 2^k), (1-e_k)^2 \mathbf{I}),$$

$$\text{Start: } \hat{\mathbf{x}}_{s_k} | \mathbf{x}_1 \sim \mathcal{N}(s_k \text{Up}(\text{Down}(\mathbf{x}_1, 2^{k+1})), (1-s_k)^2 \mathbf{I}).$$

Importantly, a single model is used to learn the velocity field in each stage, allowing knowledge sharing between stages, unlike previous cascaded approaches which require separate models for generation and superresolution [21, 22, 53].

**Pyramidal Flow Matching** Pyramidal Flow Matching [24] introduces pyramid flow matching in the video generation setting, sampling each frame with a pyramid flow autoregressively over time. This approach has important drawbacks which make it suboptimal for use in climate prediction, namely (i) the autoregressive framing leads to

slower inference runtimes, and (ii) it depends on a pre-trained VAE to perform the flow efficiently in downsampled latent space. The approach we propose in this work can sample long temporal outputs much more efficiently without the need of a VAE by using parallel, funneled generation through multiple timescales.

**PixelFlow** More recently, PixelFlow [8] adapts pyramid flows for image generation and removes the dependency on a VAE, so  $\mathbf{x}$  lies in pixel space instead of latent space. Their approach demonstrates strong performance compared to slower, higher capacity models, but does not handle temporal data nor does the formulation handle heterogeneous resampling factors, which is necessary to model data at variable timescales as we further motivate below.

## 2.2. Spatiotemporal Pyramid Flow

We introduce a class of pyramid flow models that cascade over both time and space within the flow, which we call spatiotemporal pyramid flows (SPFs). We first extend spatial pyramid flows, which previously only operate on spatial dimensions with homogeneous resampling factors, to additionally handle and parallelize over a temporal dimension, as well as support heterogeneous resampling between stages (Figure 1, § 2.2.1). To limit the high memory usage required to generate long sequences at the finest temporal resolution, we introduce a temporal funneling mechanism where we select a time period in the sequence and generate the next stage’s noisy latents from the selected period (§ 2.2.2). Finally, to allow the approach to directly generate clean samples at any of the timescales in the pyramid, we adapt the piecewise flow matching procedure to include paths in which we only change the spatial resolution while keeping the temporal resolution fixed (§ 2.2.3). Altogether, spatiotemporal pyramid flows enable temporally parallelized, direct sampling of sequences at multiple timescales, leading to efficient and accurate multiscale climate emulation (Figure 2).

### 2.2.1. Temporal Cascade and Heterogeneous Resampling

To enable temporal generation, we generalize spatial pyramid flows to handle a temporal dimension. This requires changes to the probability paths and the procedure for handling jump points between stages during inference. To address this, we derive a general expression to handle renoising with a temporal dimension and any setting of resampling factors between stages.

**Conditional Probability Path** We define a general form for the downsampling and upsampling layers for  $k = 0$  (*finest*)  $\dots K - 1$  (*coarsest*) as:

$$\begin{aligned}\text{Down}_k(\mathbf{x}) &= \text{Downsample}(\mathbf{x}, \dot{r}_k^h, \dot{r}_k^w, \dot{r}_k^t), \\ \text{Up}_k(\mathbf{z}) &= \text{Upsample}(\mathbf{z}, r_{k+1}^h, r_{k+1}^w, r_{k+1}^t).\end{aligned}$$

where  $r_k^h, r_k^w, r_k^t$  are the height, width, and temporal resampling factors between the  $k$  and  $k + 1$ th stage, and  $\dot{r}_k^h = \prod_{i=1}^k r_i^h$ ,  $\dot{r}_k^w = \prod_{i=1}^k r_i^w$ , and  $\dot{r}_k^t = \prod_{i=1}^k r_i^t$  are cumulative factors.

Then the flow within the  $k$ th time window is:

$$\mathbf{x}_t = t' \text{Down}_k(\mathbf{x}_{e_k}) + (1 - t') \text{Up}_k(\text{Down}_{k+1}(\mathbf{x}_{s_k})),$$

with the conditional probability path defined by:

$$\text{End: } \hat{\mathbf{x}}_{e_k} | \mathbf{x}_1 \sim \mathcal{N}(e_k \text{Down}_k(\mathbf{x}_1), (1 - e_k)^2 \mathbf{I}), \quad (1)$$

$$\text{Start: } \hat{\mathbf{x}}_{s_k} | \mathbf{x}_1 \sim \mathcal{N}(s_k \text{Up}_k(\text{Down}_{k+1}(\mathbf{x}_1)), (1 - s_k)^2 \mathbf{I}). \quad (2)$$

Following Jin et al. [24], we couple the sampling of the probability path endpoints by enforcing the noise to be in the same direction. That is, we sample noise  $\mathbf{n} \sim \mathcal{N}(0, \mathbf{I})$  and then jointly compute the endpoints ( $\hat{\mathbf{x}}_{e_k}, \hat{\mathbf{x}}_{s_k}$ ) with:

$$\text{End: } \hat{\mathbf{x}}_{e_k} = e_k \text{Down}_k(\mathbf{x}_1) + (1 - e_k) \mathbf{n}, \quad (3)$$

$$\text{Start: } \hat{\mathbf{x}}_{s_k} = s_k \cdot \text{Up}_k(\text{Down}_{k+1}(\mathbf{x}_1)) + (1 - s_k) \cdot \mathbf{n}. \quad (4)$$

Then we regress the flow model  $v_t$  on the conditional vector field  $u_t(\hat{\mathbf{x}}_t | \mathbf{x}_1) = \hat{\mathbf{x}}_{e_k} - \hat{\mathbf{x}}_{s_k}$  with the same flow matching objective, unifying generation and decompression:

$$\mathcal{L}_{\text{PFM}} = \mathbb{E}_{k \sim \mathcal{U}\{0, \dots, K-1\}, \substack{t \sim \mathcal{U}[s_k, e_k], \\ (\hat{\mathbf{x}}_{e_k}, \hat{\mathbf{x}}_{s_k})}} \left\| v_t(\hat{\mathbf{x}}_t) - (\hat{\mathbf{x}}_{e_k} - \hat{\mathbf{x}}_{s_k}) \right\|^2. \quad (5)$$

**Stage Continuity.** To ensure consistency at jump points between stages [6], we generalize the rescaling–renoising correction done in Jin et al. [24] to handle arbitrary per-stage resampling factors and resampling along the temporal dimension. The resulting update rule is:

$$\hat{\mathbf{x}}_{s_k} = \frac{(1 - s_k) + s_k \sqrt{n_k}}{\sqrt{n_k}} \text{Up}_k(\hat{\mathbf{x}}_{e_{k+1}}) + (1 - s_k) \sqrt{\frac{n_k - 1}{n_k}} \mathbf{n}', \quad (6)$$

where  $n_k = r_k^h r_k^w r_k^t$  and  $\mathbf{n}' \sim \mathcal{N}(0, \mathbf{I})$ . A full derivation is provided in the Appendix.

Notably, Equation (6) ensures distributional continuity across stage transitions for *any* spatial and temporal resampling factors  $r_k^h$ ,  $r_k^w$ , and  $r_k^t$  (and in fact, for any number of dimensions). Hence the pyramid can follow natural timescale hierarchies of Earth system models, e.g.  $\times 10$  from decadal to yearly but  $\times 12$  from yearly to monthly, while ensuring continuity at the jump points. In our implementation, we use  $K = 3$  stages to represent the commonly studied decadal, yearly, and monthly timescales, with  $r_k^h = r_k^w = 2$  and  $r_1^t = 10$ ,  $r_2^t = 12$ . We note that the special cases of Jin et al. [24] and Chen et al. [8] use  $r_k^h = r_k^w = 2$  and  $r_k^t = 1$ , i.e. purely spatial pyramids with homogeneous resampling factors of 2 per stage.

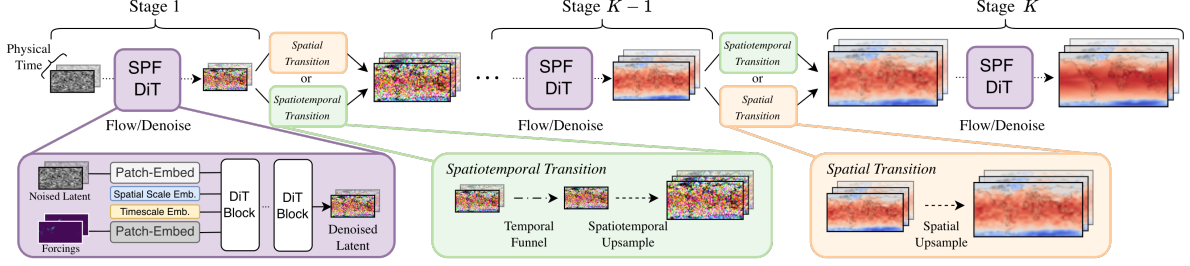


Figure 2. **SPF flow trajectory.** SPF divides generation into stages, each beginning with DiT denoising and followed by either a spatiotemporal transition (green) or a spatial-only transition (orange). Spatiotemporal transitions funnel into a timestep for the selected target period and upsample the latent in both space and time, while spatial transitions upsample only in space. This sequence of denoising and stage transitions continues until the final stage, which outputs clean samples at the target period and timescale.

### 2.2.2. Temporal Funneling

As generating a long sequence of high spatial and temporal resolution outputs at once would be prohibitively expensive, and climate use cases often only require a subset of the full sequence for downstream analysis, we propose a method to *funnel* into a time period of interest.

Specifically, we slice the latent before upsampling, saving memory and compute while still achieving probability path continuity. Because each denoised latent is Gaussian, selecting any subset of  $T'_k \leq T_k$  time indices from the denoised latent yields another Gaussian whose mean and covariance are simply the corresponding sub-vector and sub-matrix of the previous latent’s parameters. Therefore every rescaling–renoisng step derived above applies unchanged and preserves the probability path with  $T'_k$  frames instead of  $T_k$ . In our implementation, we funnel to a single frame, i.e. set  $T'_k = 1$ . Since the temporal windows contain  $T_k \in \{10, 12\}$  frames, this yields a 10 and 12 $\times$  respective reduction in GPU memory and FLOPs per stage.

### 2.2.3. Multi-Timescale Samples

Climate use cases often require outputs at varying temporal resolutions (e.g. yearly, monthly, daily), but prior pyramid flows only allow for denoised samples at the highest resolution. To circumvent the slower procedure of generating at the highest temporal resolution then averaging, we adapt training and inference to allow for direct generation of clean samples at any timescale in the cascade.

**Multi-Timescale Extension** To allow the model to output clean samples directly at any timescale in the pyramid, we augment the flow matching objective with an additional term evaluated on *temporally frozen* probability paths, where spatial resolution changes but temporal resolution remains fixed. For each training instance, we draw binary indicators  $\delta_k \sim \text{Bernoulli}(\pi_k)$  that specify whether stage  $k$  performs spatio-temporal refinement ( $\delta_k = 1$ ) or spatial-only refinement ( $\delta_k = 0$ ), subject to the constraint that once a temporal transition occurs ( $\delta_k = 1$ ), all finer stages remain temporal ( $\delta_{k'} = 1$  for  $k' > k$ ). For  $K = 3$

stages and denoting the  $k$ th timescale with  $\mathcal{T}_k$ , this produces three valid temporal paths ( $\mathcal{T}_0 \rightarrow \mathcal{T}_0 \rightarrow \mathcal{T}_0$ ,  $\mathcal{T}_0 \rightarrow \mathcal{T}_1 \rightarrow \mathcal{T}_1$ , and  $\mathcal{T}_0 \rightarrow \mathcal{T}_1 \rightarrow \mathcal{T}_2$ ). To ensure balanced coverage across these paths, we set the probabilities such that  $\delta_1 \sim \text{Bernoulli}(2/3)$  and  $\delta_2 \mid (\delta_1 = 1) \sim \text{Bernoulli}(1/2)$ , which yields equal probability for each path. In practice, this entails randomly sampling minibatches that use different flow matching pairs corresponding to the selected path. Given  $\delta_k$ , we define the per-stage temporal scaling factor

$$\tilde{r}_k^t = \begin{cases} r_k^t, & \text{if } \delta_k = 1 \quad (\text{spatiotemporal refinement}), \\ 1, & \text{if } \delta_k = 0 \quad (\text{spatial-only refinement}). \end{cases}$$

Using  $\text{Down}_k^* = \text{Downsample}(\cdot; \tilde{r}_k^h, \tilde{r}_k^w, \tilde{r}_k^t)$  and  $\text{Up}_k^* = \text{Up}(\cdot; r_{k+1}^h, r_{k+1}^w, \tilde{r}_{k+1}^t)$  to denote the downsampling and upsampling layers under the sampled path, the start–end pair for the conditional probability path is

$$\begin{aligned} \hat{\mathbf{x}}_{s_k}^* &= s_k \text{Up}_k^*(\text{Down}_{k+1}^*(\mathbf{x}_1)) + (1 - s_k)\mathbf{n}, \\ \hat{\mathbf{x}}_{e_k}^* &= e_k \text{Down}_k^*(\mathbf{x}_1) + (1 - e_k)\mathbf{n}, \end{aligned}$$

reducing to Eqs. (3)–(4) when selecting the path with spatial and temporal transitions occurring between every stage.

**Multi-Timescale Objective** With the definitions above, the multi-timescale loss is

$$\mathcal{L}_{\text{MT}} = \mathbb{E}_{k,t,\delta_k,(\hat{\mathbf{x}}_{e_k}^*, \hat{\mathbf{x}}_{s_k}^*)} \left\| \mathbf{v}_t(\hat{\mathbf{x}}_t) - (\hat{\mathbf{x}}_{e_k}^* - \hat{\mathbf{x}}_{s_k}^*) \right\|^2.$$

Because  $\delta_k$  is sampled on-the-fly, a single network is trained to denoise along any of the timescale paths.

**Inference at Coarser Timescales** At inference time, to directly sample coarser timescales (e.g. annual or decadal averages), we simply run the ODE solver up to the corresponding stage  $k^*$ , apply the rescaling–renoisng correction in Eq. (6) to handle both spatial and temporal transitions, then only run spatial upsampling, adjusting the renoisng correction accordingly, before finally denoising to generate the clean sample at the coarser timestep (Figure 2). Importantly, this procedure enables generation of coarse samples without needing to first generate the finer temporal samples.

**Spatial Scale and Timescale Embeddings** To allow the model to differentiate between stages at different spatial resolutions, we follow Jin et al. [24] and use spatial scale embeddings with a fixed sinusoidal encoding passed through a 2-layer MLP with a SiLU activation [12]. To allow the model to distinguish between inputs at different timescales with the same spatial resolution, we introduce a timescale embedding representing the current timescale of the flow. We use the same type of embedded sinusoidal encoding.

### 3. Data

#### 3.1. ClimateBench

ClimateBench [54] is a benchmark dataset derived from NorESM2-LM, including historical simulations from 1850-2015 and future CMIP6 scenarios from 2015-2100. The outputs are spatially resolved annual anomalies of surface air temperature and precipitation on a  $192 \times 288$  latitude-longitude grid, with inputs consisting of four forcing variables on a lower resolution grid ( $96 \times 144$ ): cumulative  $\text{CO}_2$  and  $\text{CH}_4$  emissions, and spatial maps of  $\text{SO}_2$  and black carbon emissions. To match our expanded dataset ClimateSuite, we additionally include a stratospheric aerosol optical depth (AOD) input which uses historical AOD for historical scenarios and is set to 0 for all future scenarios. As ClimateBench was aggregated to yearly means, we acquire the monthly data (see Appendix) to evaluate models at a finer timescale. We train all models on the historical, SSP1-2.6, and SSP5-8.5 scenarios, use SSP3-7.0 for validation, and test on SSP2-4.5 as done in previous work [38, 54].

#### 3.2. ClimateSuite

Towards training better climate emulators, we introduce ClimateSuite, the largest climate-scale ML dataset to date containing 33,739 simulation-years of data from ten climate models. With data from multiple climate models, ClimateSuite facilitates the development of superemulators, or surrogates that can emulate multiple ESMs at once. Similar to ClimateBench, it includes historical simulations and future CMIP6 scenarios for each model. We include monthly resolution data for all scenarios in the dataset as is commonly recorded in climate model outputs. Appendix Table 5 compares ClimateSuite to existing climate-scale datasets.

ClimateSuite is the first ML dataset to include simulations of SAI, a proposed intervention to reduce the impacts of climate change by adding reflective particles to the upper atmosphere to reflect a small fraction of sunlight back to space. The SAI scenarios have varying date ranges, with most SAI simulated between 2035 and 2070. Appendix Table 6 enumerates all ClimateSuite scenarios and ESMs.

The inputs and outputs in ClimateSuite match those in ClimateBench. However, because the original four variables in ClimateBench do not capture the radiative signal

from the stratospheric aerosols in SAI scenarios, we include an additional stratospheric aerosol optical depth (AOD) input, which quantifies the column-integrated extinction of sunlight by aerosols in the stratosphere. AOD thus serves as a direct proxy for the strength and spatial distribution of the forcing produced by SAI.

Because different climate models use different spatial resolutions, we interpolate all maps to the common  $192 \times 288$  latitude-longitude grid used in CESM2-WACCM. We split into train, validation, and test following the scenario split used in our ClimateBench experiments, and hold out the UKESM1-0-LL SAI experiment to test generalization to a climate model for which SAI experiments were not in the training set. As ESMs have highly variable number of ensemble members, we select 3 members per climate model to balance among them. We provide more detail about how we curate and process ClimateSuite in the Appendix.

### 4. Experiments

#### 4.1. Experimental Details

##### 4.1.1. Architecture

We use the MM-DiT architecture from SD3 [13] as the base model for all flow matching approaches. We consider two scales of the model, 100M parameters (2 layers) and 200M parameters (4 layers). We use sinusoidal position encodings [52] for the spatial dimensions following [13] and 1D Rotary Position Embeddings (RoPE) [50] for the temporal dimension following [24]. For conditioning on the inputs, we use a learnable patch embedding, add the positional embeddings, then use standard cross-attention conditioning on the flattened patchified sequence each layer of the network. We condition each stage of the flow matching approaches with temporally aligned forcings from the corresponding timescale. We use a patch size of  $8 \times 8$  for the outputs and  $16 \times 16$  for the inputs as forcings exhibit smoother spatial structure and weaker local dependencies than the outputs. To allow for efficient attention across multiple spatial and temporal resolutions within a batch, we sequence pack after patchifying [9], concatenating flattened token sequences of variable lengths (due to different spatial and temporal resolutions) along the sequence dimension. These settings together allow us train and run inference on a single NVIDIA RTX A4000 with 16GB of VRAM.

##### 4.1.2. Baselines

We compare against several baselines at the yearly and monthly timescales. At the yearly timescale, we train UNets [45], a fully fine-tuned ClimaX and ClimaX with a frozen backbone [38], a PixelFlow model [8], a PyramidalFlow model [24] which autoregressively predicts one year at a time over the course of one decade, and a single timescale version of our model that flows in parallel from noise at the



Model	Temporal Outputs	Native Timescale	Probabilistic	Yearly				Monthly			
				CRPS↓	RMSE↓	Bias ↓	Runtime (s)	CRPS↓	RMSE↓	Bias ↓	Runtime (s)
100M Parameters											
ClimaX Frozen [38]	Single	Yearly	✗	0.405	0.619	-0.014	< 1	-	-	-	-
UNet [45]	Single	Yearly	✗	0.396	0.608	-0.025	< 1	-	-	-	-
ClimaX [38]	Single	Yearly	✗	0.347	<b>0.546</b>	-0.073	< 1	-	-	-	-
Pyramidal Flow [24]	Autoregressive	Yearly	✓	0.368	0.762	-0.003	19	-	-	-	-
Multi-Yearly Flow (Ours)	Parallel	Yearly	✓	0.272	0.632	0.002	2	-	-	-	-
Multi-Monthly Flow (Ours)	Parallel	Monthly	✓	0.270	0.583	-0.129	11	<b>0.474</b>	<b>1.101</b>	-0.129	11
Pyramidal Flow [24]	Autoregressive	Monthly	✓	0.266	0.583	-0.068	84	0.501	1.137	-0.068	84
PixelFlow [8]	Single	Yearly	✓	<b>0.247</b>	<b>0.549</b>	-0.152	6	-	-	-	-
SPF (Ours)	Parallel	Multi	✓	<b>0.238</b>	0.565	0.004	3	<b>0.462</b>	<b>1.100</b>	-0.043	6
200M Parameters											
UNet [45]	Single	Yearly	✗	0.413	0.632	-0.096	1	-	-	-	-
Pyramidal Flow [24]	Autoregressive	Yearly	✓	0.327	0.671	0.035	24	-	-	-	-
Multi-Yearly Flow (Ours)	Parallel	Yearly	✓	0.254	0.595	0.002	4	-	-	-	-
Pyramidal Flow [24]	Autoregressive	Monthly	✓	0.236	0.532	-0.034	105	0.473	1.083	-0.034	105
Multi-Monthly Flow (Ours)	Parallel	Monthly	✓	0.231	0.528	0.118	21	<b>0.443</b>	<b>1.038</b>	0.118	21
PixelFlow [8]	Single	Yearly	✓	<b>0.224</b>	<b>0.504</b>	0.033	7	-	-	-	-
SPF (Ours)	Parallel	Multi	✓	<b>0.222</b>	<b>0.511</b>	-0.049	6	<b>0.453</b>	<b>1.060</b>	-0.063	11

Table 1. **ClimateBench test metrics on held-out scenario (SSP2-4.5).** Models use identical DiT backbones except for the UNet and ClimaX models, for which we match number of parameters. We **bold** the top two results per parameter count and timescale. We report the runtime required to sample a single 10-year trajectory at each timescale on a single NVIDIA RTX 6000.

yearly timescale to clean yearly samples spanning a decade, without any temporal funneling or resampling, which we refer to as Multi-Yearly Flow. The UNet, ClimaX, and PixelFlow models are non-temporal and output one year at a time independently. At the monthly timescale, we train a PyramidalFlow model [24] which autoregressively predicts one month at a time over the course of one year. We also train a Multi-Monthly Flow which operates analogously to the Multi-Yearly Flow but instead generates monthly samples spanning a year. Therefore the Multi-Yearly and Multi-Monthly flow models output 10 and 12 frames respectively, matching SPF. We note all flow matching approaches operate in pixel space. To control for model capacity, we match the number of parameters of the UNet and use the same backbone architectures for the flow matching approaches.

#### 4.1.3. Evaluation Procedure

We evaluate with three standard metrics, namely root mean squared error (RMSE), bias, and continuous ranked probability score (CRPS). We weight all metrics by grid cell area, formally defined in the Appendix. RMSE and bias measure the quality of the mean prediction whereas CRPS captures the probabilistic skill of the model by assessing both the accuracy and sharpness of the predicted distribution relative to the targets. We evaluate the probabilistic models using 5 samples and standardize to 90 inference steps total, split equally by stage, using an Euler solver.

We evaluate the models at both monthly and yearly timescales. While we cannot evaluate the native yearly models at the monthly timescale, we additionally evaluate the native monthly models at the yearly timescale by averaging across the calendar year.

## 4.2. Results

### 4.2.1. SPF Comparison to Baselines

SPF achieves the lowest CRPS compared to all 100M and 200M parameter models respectively at the yearly timescale (Table 1). SPF with 200M params has the second lowest RMSE, close behind the yearly PixelFlow model and considerably ahead of all other 200M param models. With 100M params, it achieves slightly poorer RMSE than the single year PixelFlow and ClimaX models but outperforms all other approaches. We emphasize that ClimaX is a strong model pre-trained on a large climate dataset whereas SPF is only trained on the ClimateBench training set. SPF’s bias is close to perfect at the yearly timescale with 100M params, and comparable to other approaches with 200M params. Importantly, it achieves this high performance with very efficient sampling: the 100M and 200M variants achieve  $28\times$  and  $> 15\times$  speedups respectively compared to the autoregressive PyramidalFlow model, reducing sampling time down to a few seconds.

At the monthly timescale, SPF with 100M params achieves the best CRPS, RMSE, and bias, and the 200M param model achieves the lowest RMSE and close to best CRPS. Sampling 10 years of monthly outputs is  $> 3\times$  faster than PyramidalFlow with 200M params and  $6\times$  faster with 100M. We plot SPF’s monthly and yearly global means, histograms, and monthly and yearly samples compared to the simulation data in the Appendix.

### 4.2.2. Pyramid Design Ablation

We explore alternate pyramid designs of SPF. We consider an approach that uses the same three stage decadal  $\rightarrow$  yearly  $\rightarrow$  monthly design as SPF, but only trained to support clean

Variant	Stage Sequence	CRPS↓	RMSE↓
DYMMM	Dec → Yr → Mo → Mo → Mo	0.474	1.087
DYYMM	Dec → Yr → Yr → Mo → Mo	0.463	1.085
DYM-Monthly	Dec → Yr → Mo	0.453	1.064
SPF (DYM-Any)	Dec → Yr → Mo	<b>0.453</b>	<b>1.060</b>

Table 2. **Ablation study on the design of the spatiotemporal pyramid on ClimateBench SSP2-4.5 (monthly timescale).** SPF (DYM-Any) supports samples at any of the timescales, whereas the other variants only support monthly samples. All variants use an identical DiT architecture with 200M parameters.

ClimateSuite Pretrained	Parameters	Yearly		Monthly	
		CRPS	RMSE	CRPS	RMSE
-	200M	0.222	0.511	0.453	1.060
-	600M	0.229	0.523	0.442	1.053
✓	600M	<b>0.216</b>	<b>0.491</b>	<b>0.432</b>	<b>1.026</b>

Table 3. **Effect of scale and ClimateSuite pre-training on ClimateBench performance.**

monthly samples (DYM-Monthly). We also train two variants with decoupled spatial and temporal transitions, one starting with the temporal transitions and then ending with the spatial ones (DYMMM), and one where we alternate temporal and spatial transitions (DYYMM). We note that we considered an alternating pyramid that starts with spatial then temporal but this variant ran out of GPU memory.

SPF’s design outperforms all other tested variants (Table 2). The 3 stage design without multi-scale sampling (DYM-Monthly) achieves similar CRPS but slightly higher RMSE than the SPF design (DYM-Any), indicating there is a small improvement to the monthly sampling performance when training the model to support sampling from the other timescales. The 5 stage variants underperform both 3 stage variants, with the alternating approach (DYYMM) outperforming the design starting with the temporal transitions (DYMMM).

#### 4.2.3. Scaled SPF Multi-Model Results

To investigate the impact of scale and ClimateSuite pre-training, we train a 600M parameter SPF model on ClimateSuite then fine-tune it on ClimateBench. We find that scale and pre-training together lead to improvements across the yearly and monthly timescales (Table 3). This gain is not only due to scale, as a 600M parameter non-pre-trained model underperforms the 200M parameter variant at the yearly timescale, and the pre-trained model outperforms the non-pre-trained model on both timescales.

We additionally evaluate SPF against a 600M-parameter UNet explored previously for multi-model emulation [25] on the held-out SSP scenario across 10 climate models and the held-out SAI scenario on UKESM1-0-LL. SPF achieves superior performance across all climate models (Table 4).

Climate Model	RMSE ↓		CRPS ↓	
	UNet	SPF	UNet	SPF
<i>Standard scenario (SSP2-4.5)</i>				
BCC-CSM2-MR	0.770	<b>0.749</b>	0.491	<b>0.311</b>
CESM2	0.523	<b>0.473</b>	0.326	<b>0.224</b>
CESM2-WACCM	0.521	<b>0.468</b>	0.332	<b>0.216</b>
CMCC-CM2-SR5	0.842	<b>0.745</b>	0.539	<b>0.318</b>
CMCC-ESM2	0.886	<b>0.817</b>	0.552	<b>0.347</b>
GFDL-ESM4	0.520	<b>0.483</b>	0.320	<b>0.223</b>
IPSL-CM6A-LR	0.544	<b>0.432</b>	0.330	<b>0.200</b>
MRI-ESM2-0	0.540	<b>0.502</b>	0.347	<b>0.230</b>
NorESM2-LM	0.536	<b>0.491</b>	0.350	<b>0.226</b>
UKESM1-0-LL	0.599	<b>0.561</b>	0.343	<b>0.261</b>
Average	0.616	<b>0.573</b>	0.393	<b>0.256</b>
<i>Intervention scenario (SAI)</i>				
UKESM1-0-LL	0.883	<b>0.727</b>	0.466	<b>0.315</b>

Table 4. **Yearly metrics on held-out scenarios across climate models in ClimateSuite.** CRPS is evaluated using 5 ensemble members. Both UNet and SPF use 600M parameters. We **bold** the better value per row.

Notably, on the held-out SAI scenario, SPF generates samples with global means close to the simulations in most of the century, with poorer performance at the start. However, we note that this is achieved without training on any SAI data from UKESM1-0-LL. We plot global means, histograms, and samples per model compared to the ground truth simulations in the Appendix.

## 5. Conclusion

We introduce SPF, a new flow matching approach to model spatiotemporal data at multiple timescales. Our results show that SPF is an efficient and accurate probabilistic climate emulator, enabling scalable and high-fidelity modeling of multiple ESMs, future scenarios, and timescales. We also curate ClimateSuite, the largest ML-ready climate-scale dataset. We hope that ClimateSuite will serve as a valuable resource to train multi-model superemulators and help mitigate the overfitting observed in prior models trained on the much smaller ClimateBench dataset [35]. Together, SPF and ClimateSuite advance the development of scalable, probabilistic emulators for ESMs.

Our work has limitations. First, SPF does not explicitly enforce physical constraints such as energy or mass conservation, which may yield physically inconsistent trajectories under some forcing conditions. Second, while ClimateSuite spans multiple models and scenarios, it is constrained to existing ESM ensembles, likely limiting generalization to unseen parameterizations or extreme forcings. Future work should explore ways to overcome these limitations.

## References

- [1] Bouwe Andela, Bjoern Broetz, Lee de Mora, Niels Drost, Veronika Eyring, Nikolay Koldunov, Axel Lauer, Valeriu Predoi, Mattia Righi, Manuel Schlund, Javier Vegas-Regidor, Klaus Zimmermann, Lisa Bock, Faruk Diblen, Laura Dreyer, Paul Earnshaw, Birgit Hassler, Bill Little, Saskia Loosveldt-Tomas, Stef Smeets, Jaro Camphuijsen, Bettina K. Gier, Katja Weigel, Mathias Hauser, Peter Kalverla, Evgenia Galytska, Pep Cos-Espuña, Inti Pelupessy, Sujan Koirala, Tobias Stacke, Sarah Alidoost, Martin Jury, Stéphane Sénési, Thomas Crocker, Barbara Vreede, Abel Soares Siqueira, Rémi Kazeroni, David Hohn, Julian Bauer, Romain Beucher, Joerg Benke, Eneko Martin-Martinez, Diego Cammarano, Zeng Yousong, Elizaveta Malinina, Karen Garcia Perdomo, and Julien Lenhardt. ESM-ValCore, 2025. [14](#)
- [2] Seth Basseti, Brian Hutchinson, Claudia Tebaldi, and Ben Kravitz. DiffESM: Conditional emulation of temperature and precipitation in earth system models with 3d diffusion models. *Journal of Advances in Modeling Earth Systems*, 16(10):e2023MS004194, 2024. [12](#)
- [3] Shahine Bouabid, Dino Sejdinovic, and Duncan Watson-Parris. Fairgp: A bayesian energy balance model for surface temperatures emulation. *Journal of Advances in Modeling Earth Systems*, 16(6):e2023MS003926, 2024. [2](#)
- [4] Noah D. Brenowitz, Tao Ge, Akshay Subramaniam, Peter Manshausen, Aayush Gupta, David M. Hall, Morteza Mardani, Arash Vahdat, Karthik Kashinath, and Michael S. Pritchard. Climate in a bottle: Towards a generative foundation model for the kilometer-scale global atmosphere. *arXiv preprint arXiv:2505.06474*, 2025. [12](#)
- [5] Salva Rühling Cachay, Brian Henn, Oliver Watt-Meyer, Christopher S. Bretherton, and Rose Yu. Probabilistic emulation of a global climate model with spherical DYffusion. In *Advances in Neural Information Processing Systems (NeurIPS)*, 2024. [1](#), [2](#), [12](#), [14](#)
- [6] Andrew Campbell, William Harvey, Christian Weillbach, Valentin De Bortoli, Thomas Rainforth, and Arnaud Doucet. Trans-dimensional generative modeling via jump diffusion models. *Advances in Neural Information Processing Systems*, 36:42217–42257, 2023. [4](#)
- [7] Boyuan Chen, Diego Martí Monsó, Yilun Du, Max Simchowitz, Russ Tedrake, and Vincent Sitzmann. Diffusion forcing: Next-token prediction meets full-sequence diffusion. *Advances in Neural Information Processing Systems*, 37:24081–24125, 2024. [2](#)
- [8] Shoufa Chen, Chongjian Ge, Shilong Zhang, Peize Sun, and Ping Luo. Pixelflow: Pixel-space generative models with flow. *arXiv preprint arXiv:2504.07963*, 2025. [2](#), [3](#), [4](#), [6](#), [7](#), [12](#), [16](#)
- [9] Mostafa Dehghani, Basil Mustafa, Josip Djolonga, Jonathan Heek, Matthias Minderer, Mathilde Caron, Andreas Steiner, Joan Puigcerver, Robert Geirhos, Ibrahim M Alabdulmohsin, et al. Patch n’pack: Navit, a vision transformer for any aspect ratio and resolution. *Advances in Neural Information Processing Systems*, 36:2252–2274, 2023. [6](#)
- [10] Prafulla Dhariwal and Alexander Nichol. Diffusion models beat gans on image synthesis. *Advances in neural information processing systems*, 34:8780–8794, 2021. [12](#)
- [11] Laurent Dinh, Jascha Sohl-Dickstein, and Samy Bengio. Density estimation using real nvp. *arXiv preprint arXiv:1605.08803*, 2016. [12](#)
- [12] Stefan Elfving, Eiji Uchibe, and Kenji Doya. Sigmoid-weighted linear units for neural network function approximation in reinforcement learning. *Neural networks*, 107:3–11, 2018. [6](#)
- [13] Patrick Esser, Sumith Kulal, Andreas Blattmann, Rahim Entezari, Jonas Müller, Harry Saini, Yam Levi, Dominik Lorenz, Axel Sauer, Frederic Boesel, et al. Scaling rectified flow transformers for high-resolution image synthesis. In *Forty-first international conference on machine learning*, 2024. [6](#)
- [14] Veronika Eyring, Sandrine Bony, Gerald A Meehl, Catherine A Senior, Bjorn Stevens, Ronald J Stouffer, and Karl E Taylor. Overview of the coupled model intercomparison project phase 6 (cmip6) experimental design and organization. *Geoscientific Model Development*, 9(5):1937–1958, 2016. [1](#)
- [15] Piers M. Forster, Luke S. Jackson, Chris J. Smith, Joeri Rogelj, et al. The role of climate model emulators in ipcc ar6. Technical report, CONSTRAIN EU Project, 2021. Used for global mean temperature and sea level projections at annual timescales. [1](#)
- [16] Mark Govett, Bubacar Bah, Peter Bauer, Dominique Berod, Veronique Bouchet, Susanna Corti, Chris Davis, Yihong Duan, Tim Graham, Yuki Honda, et al. Exascale computing and data handling: Challenges and opportunities for weather and climate prediction. *Bulletin of the American Meteorological Society*, 105(12):E2385–E2404, 2024. [1](#)
- [17] Yoav HaCohen, Nisan Chiprut, Benny Brazowski, Daniel Shalem, Dudu Moshe, Eitan Richardson, Eran Levin, Guy Shiran, Nir Zabari, Ori Gordon, et al. Ltx-video: Realtime video latent diffusion. *arXiv preprint arXiv:2501.00103*, 2024. [2](#)
- [18] Taufiq Hassan. acccmip6: Python package for accessing and downloading CMIP6 data, 2022. [14](#)
- [19] Hans Hersbach, Bill Bell, Paul Berrisford, Shoji Hirahara, András Horányi, Joaquín Muñoz-Sabater, Julien Nicolas, Carole Peubey, Raluca Radu, Dinand Schepers, et al. The era5 global reanalysis. *Quarterly journal of the royal meteorological society*, 146(730):1999–2049, 2020. [14](#)
- [20] Jonathan Ho, Ajay Jain, and Pieter Abbeel. Denoising diffusion probabilistic models. *Advances in neural information processing systems*, 33:6840–6851, 2020. [2](#), [3](#), [12](#)
- [21] Jonathan Ho, William Chan, Chitwan Saharia, Jay Whang, Ruiqi Gao, Alexey Gritsenko, Diederik P. Kingma, Ben Poole, Mohammad Norouzi, David J. Fleet, and Tim Salimans. Imagen video: High definition video generation with diffusion models, 2022. *arXiv preprint arXiv:2210.02303*. [3](#)
- [22] Jonathan Ho, Chitwan Saharia, William Chan, David J Fleet, Mohammad Norouzi, and Tim Salimans. Cascaded diffusion models for high fidelity image generation. *Journal of Machine Learning Research*, 23(47):1–33, 2022. [2](#), [3](#), [12](#)

- [23] Jonathan Ho, Tim Salimans, Alexey Gritsenko, William Chan, Mohammad Norouzi, and David J Fleet. Video diffusion models. *Advances in neural information processing systems*, 35:8633–8646, 2022. 2, 12
- [24] Yang Jin, Zhicheng Sun, Ningyuan Li, Kun Xu, Hao Jiang, Nan Zhuang, Quzhe Huang, Yang Song, Yadong Mu, and Zhouchen Lin. Pyramidal flow matching for efficient video generative modeling. *arXiv preprint arXiv:2410.05954*, 2024. 2, 3, 4, 6, 7, 12, 13, 16
- [25] Julia Kaltenborn, Charlotte Lange, Venkatesh Ramesh, Philippe Brouillard, Yaniv Gurwicz, Chandni Nagda, Jakob Runge, Peer Nowack, and David Rolnick. Climateset: A large-scale climate model dataset for machine learning. *Advances in Neural Information Processing Systems*, 36: 21757–21792, 2023. 8, 14
- [26] Jennifer E Kay, Clara Deser, A Phillips, A Mai, Cecile Hannay, Gary Strand, Julie Michelle Arblaster, SC Bates, Gokhan Danabasoglu, James Edwards, et al. The community earth system model (cesm) large ensemble project: A community resource for studying climate change in the presence of internal climate variability. *Bulletin of the American Meteorological Society*, 96(8):1333–1349, 2015. 1
- [27] Durk P Kingma and Prafulla Dhariwal. Glow: Generative flow with invertible 1x1 convolutions. *Advances in neural information processing systems*, 31, 2018. 12
- [28] Dmitrii Kochkov, Janni Yuval, Ian Langmore, Peter Norgaard, Jamie Smith, Griffin Mooers, Milan Klöwer, James Lottes, Stephan Rasp, Peter Düben, et al. Neural general circulation models for weather and climate. *Nature*, 632(8027): 1060–1066, 2024. 1, 2
- [29] Weijie Kong, Qi Tian, Zijian Zhang, Rox Min, Zuozhuo Dai, Jin Zhou, Jiangfeng Xiong, Xin Li, Bo Wu, Jianwei Zhang, et al. Hunyuanvideo: A systematic framework for large video generative models. *arXiv preprint arXiv:2412.03603*, 2024. 2
- [30] Ben Kravitz, Alan Robock, Simone Tilmes, Olivier Boucher, Jason M English, Peter J Irvine, Andy Jones, Mark G Lawrence, Michael MacCracken, Helene Muri, et al. The geoeengineering model intercomparison project phase 6 (geomip6): Simulation design and preliminary results. *Geoscientific Model Development*, 8(10):3379–3392, 2015. 1
- [31] Fenghua Ling, Zeyu Lu, Jing-Jia Luo, Lei Bai, Swadhin K Behera, Dachao Jin, Baoxiang Pan, Huidong Jiang, and Toshio Yamagata. Diffusion model-based probabilistic downscaling for 180-year east asian climate reconstruction. *npj Climate and Atmospheric Science*, 7(1):131, 2024. 12
- [32] Yaron Lipman, Ricky TQ Chen, Heli Ben-Hamu, Maximilian Nickel, and Matt Le. Flow matching for generative modeling. *arXiv preprint arXiv:2210.02747*, 2022. 2, 3, 12
- [33] Ruyang Liu, Chen Li, Haoran Tang, Yixiao Ge, Ying Shan, and Ge Li. St-llm: Large language models are effective temporal learners. In *European Conference on Computer Vision*, pages 1–18. Springer, 2024. 2
- [34] Xingchao Liu, Chengyue Gong, and Qiang Liu. Flow straight and fast: Learning to generate and transfer data with rectified flow. *arXiv preprint arXiv:2209.03003*, 2022. 3
- [35] Björn Lütjens, Raffaele Ferrari, Duncan Watson-Parris, and Noelle E Selin. The impact of internal variability on benchmarking deep learning climate emulators. *Journal of Advances in Modeling Earth Systems*, 17(8):e2024MS004619, 2025. 8
- [36] James E Matheson and Robert L Winkler. Scoring rules for continuous probability distributions. *Management science*, 22(10):1087–1096, 1976. 15
- [37] Met Office. UKESM1-0 ARISE-SAI information and CMOR3 tables (arise-cmor-tables). <https://github.com/MetOffice/arise-cmor-tables>, 2025. Accessed: 2025-11-12. 14
- [38] Tung Nguyen, Johannes Brandstetter, Ashish Kapoor, Jayesh K Gupta, and Aditya Grover. Climax: A foundation model for weather and climate. *arXiv preprint arXiv:2301.10343*, 2023. 6, 7, 14, 16
- [39] Ruijia Niu, Dongxia Wu, Kai Kim, Yi-An Ma, Duncan Watson-Parris, and Rose Yu. Multi-fidelity residual neural processes for scalable surrogate modeling. *arXiv preprint arXiv:2402.18846*, 2024. 1
- [40] Brian C O’Neill, Claudia Tebaldi, Detlef P Van Vuuren, Veronika Eyring, Pierre Friedlingstein, George Hurtt, Reto Knutti, Elmar Kriegler, Jean-Francois Lamarque, Jason Lowe, et al. The scenario model intercomparison project (scenariomip) for cmip6. *Geoscientific Model Development*, 9(9):3461–3482, 2016. 1
- [41] Derek Onken, Samy Wu Fung, Xingjian Li, and Lars Ruthotto. Ot-flow: Fast and accurate continuous normalizing flows via optimal transport. In *Proceedings of the AAAI Conference on Artificial Intelligence*, pages 9223–9232, 2021. 3
- [42] George Papamakarios, Eric Nalisnick, Danilo Jimenez Rezende, Shakir Mohamed, and Balaji Lakshminarayanan. Normalizing flows for probabilistic modeling and inference. *Journal of Machine Learning Research*, 22(57):1–64, 2021. 3
- [43] Adam Polyak, Amit Zohar, Andrew Brown, Andros Tjandra, Animesh Sinha, Ann Lee, Apoorv Vyas, Bowen Shi, Chih-Yao Ma, Ching-Yao Chuang, et al. Movie gen: A cast of media foundation models. *arXiv preprint arXiv:2410.13720*, 2024. 2
- [44] Stephan Rasp, Peter D Dueben, Sebastian Scher, Jonathan A Weyn, Soukayna Mouatadid, and Nils Thuerey. Weather-bench: a benchmark data set for data-driven weather forecasting. *Journal of Advances in Modeling Earth Systems*, 12(11):e2020MS002203, 2020. 14
- [45] Olaf Ronneberger, Philipp Fischer, and Thomas Brox. U-net: Convolutional networks for biomedical image segmentation. In *International Conference on Medical image computing and computer-assisted intervention*, pages 234–241. Springer, 2015. 6, 7, 16
- [46] Chitwan Saharia, Jonathan Ho, William Chan, Tim Salimans, David J Fleet, and Mohammad Norouzi. Image super-resolution via iterative refinement. *IEEE transactions on pattern analysis and machine intelligence*, 45(4):4713–4726, 2022. 12
- [47] Jascha Sohl-Dickstein, Eric Weiss, Niru Maheswaranathan, and Surya Ganguli. Deep unsupervised learning using nonequilibrium thermodynamics. In *International conference on machine learning*, pages 2256–2265. pmlr, 2015. 3



- [48] Yang Song and Stefano Ermon. Generative modeling by estimating gradients of the data distribution. *Advances in neural information processing systems*, 32, 2019. [3](#), [12](#)
- [49] Prakhar Srivastava, Ruihan Yang, Gavin Kerrigan, Gideon Dresdner, and Jeremy McGibbon. Precipitation downscaling with spatiotemporal video diffusion. In *Advances in Neural Information Processing Systems (NeurIPS)*, 2024. [12](#)
- [50] Jianlin Su, Murtadha Ahmed, Yu Lu, Shengfeng Pan, Wen Bo, and Yunfeng Liu. Roformer: Enhanced transformer with rotary position embedding. *Neurocomputing*, 568:127063, 2024. [6](#)
- [51] Claudia Tebaldi, NE Selin, R Ferrari, and G Flierl. Emulators of climate model output. *Annual Review of Environment and Resources*, 50, 2025. [1](#)
- [52] Ashish Vaswani, Noam Shazeer, Niki Parmar, Jakob Uszkoreit, Llion Jones, Aidan N Gomez, Łukasz Kaiser, and Illia Polosukhin. Attention is all you need. *Advances in neural information processing systems*, 30, 2017. [6](#)
- [53] Yaohui Wang, Xinyuan Chen, Xin Ma, Shangchen Zhou, Ziqi Huang, Yi Wang, Ceyuan Yang, Yinan He, Jiashuo Yu, Peiqing Yang, et al. Lavie: High-quality video generation with cascaded latent diffusion models. *International Journal of Computer Vision*, 133(5):3059–3078, 2025. [3](#)
- [54] Duncan Watson-Parris, Y. Rao, Delphine Olivie, Øyvind Seland, Peer Nowack, Gustau Camps-Valls, Philip Stier, and et al. ClimateBench v1.0: a benchmark for data-driven climate projections. *Journal of Advances in Modeling Earth Systems*, 14(10):e2021MS002954, 2022. [1](#), [2](#), [6](#), [14](#)
- [55] Robbie A Watt and Laura A Mansfield. Generative diffusion-based downscaling for climate. *arXiv preprint arXiv:2404.17752*, 2024. [12](#)
- [56] Oliver Watt-Meyer, Gideon Dresdner, Jeremy McGibbon, Spencer K. Clark, Brian Henn, James Duncan, Noah D. Brenowitz, Karthik Kashinath, Michael S. Pritchard, Boris Bonev, Matthew E. Peters, and Christopher S. Bretherton. ACE: A fast, skillful learned global atmospheric model for climate prediction. *arXiv preprint arXiv:2310.02074*, 2024. [1](#), [14](#)
- [57] Oliver Watt-Meyer, Brian Henn, Jeremy McGibbon, Spencer K Clark, Anna Kwa, W Andre Perkins, Elynn Wu, Lucas Harris, and Christopher S Bretherton. Ace2: accurately learning subseasonal to decadal atmospheric variability and forced responses. *npj Climate and Atmospheric Science*, 8(1):205, 2025. [1](#)
- [58] Hanshu Yan, Xingchao Liu, Jiachun Pan, Jun Hao Liew, Qiang Liu, and Jiashi Feng. Perflow: Piecewise rectified flow as universal plug-and-play accelerator. *arXiv preprint arXiv:2405.07510*, 2024. [3](#)
- [59] Daquan Zhou, Weimin Wang, Hanshu Yan, Weiwei Lv, Yizhe Zhu, and Jiashi Feng. Magicvideo: Efficient video generation with latent diffusion models. *arXiv preprint arXiv:2211.11018*, 2022. [12](#)

## Appendix Outline

<b>A Related Work</b>	<b>12</b>
A.1 Diffusion and Flow Matching Models . . . .	12
A.2 Generative Models for Climate . . . . .	12
<b>B Rescaling and Renoising for Probability Path Continuity</b>	<b>12</b>
B.1 Spatial-Only Derivation . . . . .	12
B.2 Temporal and Heterogeneous Resampling Derivation . . . . .	13
<b>C ClimateSuite Dataset</b>	<b>13</b>
C.1 Climate Model and Scenario Selection . . . .	13
C.2 Simulation Downloading . . . . .	14
C.3 Data Processing . . . . .	14
<b>D Evaluation Metrics</b>	<b>14</b>
D.1 Preliminaries . . . . .	14
D.2 Metric definitions . . . . .	14
<b>E Additional Results</b>	<b>15</b>
E.1 Long Sequence Runtimes . . . . .	15
E.2 Other Results . . . . .	16

## A. Related Work

### A.1. Diffusion and Flow Matching Models

Diffusion models have become a cornerstone of generative modeling, framing synthesis as the reversal of a gradual noising process through learned score functions [20, 48]. Subsequent work extended this paradigm to conditional and guided settings, achieving state-of-the-art image generation [10] and later to spatiotemporal domains via video diffusion and latent video variants for efficient long-horizon synthesis [23, 59]. To further scale quality and resolution, cascaded diffusion pipelines decompose generation into multi-stage refinement processes, where coarse outputs are progressively upsampled by higher-resolution diffusion models [22, 46]. Flow-based models offer an alternative by learning invertible mappings from noise to data with exact likelihoods [11, 27], and the introduction of flow matching unified flow and diffusion training through deterministic ODE trajectories between distributions [32]. Recent hierarchical flow architectures extend this principle across scales: PyramidalFlow [24] and PixelFlow [8] use pyramids of flows at increasing spatial or spatiotemporal resolutions to more efficiently model video and image data respectively.

### A.2. Generative Models for Climate

Generative AI has increasingly been applied in climate science to emulate expensive simulations and enhance spatial resolution. Diffusion models, in particular, have shown

strong potential for generating realistic spatiotemporal climate fields. Several previous works have demonstrated that diffusion models can be used for downscaling, to enhance coarse reanalysis and model fields to higher resolutions Ling et al. [31], Srivastava et al. [49], Watt and Mansfield [55]. DiffESM applies conditional diffusion to produce daily climate variables consistent with coarse monthly means [2]. Climate in a Bottle (cBottle) proposes a two-stage diffusion framework that first synthesizes coarse 100 km atmospheric fields before applying a learned diffusion-based super-resolution to reach kilometer scales [4]. Spherical DYffusion introduces a weather-scale probabilistic emulator based on a dynamics-informed ‘dyffusion’ process paired with a spherical Fourier neural operator, enabling stable long-horizon global climate emulation of a simplified atmospheric model with fixed forcings [5].

## B. Rescaling and Renoising for Probability Path Continuity

We derive the rescaling-renoising correction described in Equation 6 to handle the additional temporal dimension and support heterogeneous resampling factors between stages.

### B.1. Spatial-Only Derivation

We will start with the simpler spatial-only, homogeneous resampling setting presented in Section 2.1.3 and rederive the intermediate steps from Jin et al. [24] here for clarity. Following Jin et al. [24], we upsample the previous low-resolution endpoint using nearest-neighbor resampling, resulting in a linear combination of the inputs, which therefore follows a Gaussian distribution:

$$\text{Up}_k(\hat{\mathbf{x}}^{e_{k+1}}) \mid \mathbf{x}_1 \sim \mathcal{N}(e_{k+1} \text{Up}_k(\text{Down}_{k+1}(\mathbf{x}_1)), (1 - e_{k+1})^2 \Sigma), \quad (7)$$

with  $\Sigma$  is the covariance matrix induced by the upsampling operation.

To ensure continuity of the probability path between different stages of the spatial pyramid, the endpoints must have the same distributions. Eqs. (1), (2), and (7) show that the distributions of the endpoints are similar after a simple upsampling transformation:

$$\hat{\mathbf{x}}_{s_k} \mid \mathbf{x}_1 \sim \mathcal{N}(s_k \text{Up}_k(\text{Down}_{k+1}(\mathbf{x}_1)), (1 - s_k)^2 I) \quad (8)$$

$$\text{Up}_k(\hat{\mathbf{x}}_{e_{k+1}}) \mid \mathbf{x}_1 \sim \mathcal{N}(e_{k+1} \text{Up}_k(\text{Down}_{k+1}(\mathbf{x}_1)), (1 - e_{k+1})^2 \Sigma). \quad (9)$$

We can therefore apply a linear transformation with a corrective Gaussian noise to match the distributions:

$$\hat{\mathbf{x}}_{s_k} = \frac{s_k}{e_{k+1}} \text{Up}_k(\hat{\mathbf{x}}_{e_{k+1}}) + \alpha \mathbf{n}', \quad \text{where } \mathbf{n}' \sim \mathcal{N}(0, \Sigma'). \quad (10)$$

The rescaling coefficient  $\frac{s_k}{e_{k+1}}$  matches the means of these distributions, and  $\alpha$  is the noise coefficient. To determine  $\alpha$  and  $\Sigma'$ , we need to match the covariance matrices of Eqs. (8) and (10)

$$\frac{s_k^2}{e_{k+1}^2}(1 - e_{k+1})^2 \Sigma + \alpha^2 \Sigma' = (1 - s_k)^2 \mathbf{I}. \quad (11)$$

Jin et al. [24] show that for a simple nearest neighbor up-sampling operation,  $\Sigma$  and  $\Sigma'$  have blockwise structure that can be exploited to determine the noise correction to match the endpoint distributions.

## B.2. Temporal and Heterogeneous Resampling Derivation

We now consider the setting presented in Section 2.2.1. We generalize these covariance matrices to any differing, per-stage resampling factors  $r_k^h$ ,  $r_k^w$ , and  $r_k^t$  by allowing per-stage upsampling covariance matrices  $\Sigma_k$  and corrective noise covariance matrices  $\Sigma'_k$  as well as per-stage corrective noise coefficients  $\alpha_k$ . Rewriting Eqs (10) and (11),

$$\hat{\mathbf{x}}_{s_k} = \frac{s_k}{e_{k+1}} \text{Up}_k(\hat{\mathbf{x}}_{e_{k+1}}) + \alpha_k \mathbf{n}', \quad \text{where } \mathbf{n}' \sim \mathcal{N}(0, \Sigma'_k). \quad (12)$$

$$\frac{s_k^2}{e_{k+1}^2}(1 - e_{k+1})^2 \Sigma_k + \alpha_k^2 \Sigma'_k = (1 - s_k)^2 \mathbf{I}. \quad (13)$$

Importantly, the per-stage covariance matrices remain  $n_k \times n_k$  block diagonal with  $n_k = r_k^h \cdot r_k^w \cdot r_k^t$ .

$$\begin{aligned} (\Sigma_k)_{\text{block}} &= \mathbf{J}_n = \begin{pmatrix} 1 & 1 & \dots & 1 \\ 1 & \ddots & \ddots & \vdots \\ \vdots & \ddots & \ddots & 1 \\ 1 & \dots & 1 & 1 \end{pmatrix}, \\ \Rightarrow (\Sigma'_k)_{\text{block}} &= \begin{pmatrix} 1 & \gamma_k & \dots & \gamma_k \\ \gamma_k & \ddots & \ddots & \vdots \\ \vdots & \ddots & \ddots & \gamma_k \\ \gamma_k & \dots & \gamma_k & 1 \end{pmatrix}. \end{aligned} \quad (14)$$

where  $\gamma_k$  is a negative value in  $[-\frac{1}{n_k-1}, 0]$  for decorrelation, and its lower bound ensures that the covariance matrix is positive semidefinite i.e. forms an equicorrelation matrix.

We can then rewrite Eqs. (13) and (14) by equating their diagonal and non-diagonal elements respectively:

$$\begin{aligned} \frac{s_k^2}{e_{k+1}^2}(1 - e_{k+1})^2 + \alpha_k^2 &= (1 - s_k)^2, \\ \frac{s_k^2}{e_{k+1}^2}(1 - e_{k+1})^2 + \alpha_k^2 \gamma_k &= 0. \end{aligned}$$

Since  $0 < s_k, e_{k+1} < 1$ , the equations are solvable with:

$$e_{k+1} = \frac{s_k \sqrt{1 - \gamma_k}}{(1 - s_k) \sqrt{-\gamma_k} + s_k \sqrt{1 - \gamma_k}}, \quad \alpha_k = \frac{1 - s_k}{\sqrt{1 - \gamma_k}}. \quad (15)$$

Intuitively, we want to preserve signals maximally at each jump point, which corresponds to minimizing the noise weight  $\alpha_k$ . According to Eq. (15), this is equivalent to minimizing  $\gamma_k$  at each jump point. Substituting the minimum value  $\gamma_k = -\frac{1}{n_k-1}$  into Eq. (15) yields:

$$e_{k+1} = \frac{s_k \sqrt{n_k}}{(1 - s_k) + s_k \sqrt{n_k}}, \quad \alpha_k = (1 - s_k) \sqrt{\frac{n_k - 1}{n_k}}$$

As in Jin et al. [24], we find that  $e_{k+1} > s_k$  in this generalized form, meaning the timestep is rolled back when adding the corrective noise at each jump point. Substituting this back into equation (12) yields

$$\begin{aligned} \hat{\mathbf{x}}_{s_k} &= \frac{s_k}{e_{k+1}} \text{Up}_k(\hat{\mathbf{x}}_{e_{k+1}}) + \alpha_k \mathbf{n}' \\ &= \frac{(1 - s_k) + s_k \sqrt{n_k}}{\sqrt{n_k}} \text{Up}_k(\hat{\mathbf{x}}_{e_{k+1}}) + (1 - s_k) \sqrt{\frac{n_k - 1}{n_k}} \mathbf{n}' \end{aligned}$$

matching the update rule presented in Eq. (6).

## C. ClimateSuite Dataset

### C.1. Climate Model and Scenario Selection

We select ten CMIP6 Earth system models to ensure broad coverage across model families, physical parameterizations, and scenario availability (Table S2). We include NorESM2-LM specifically because it is the reference model used in ClimateBench, enabling direct comparison with prior benchmarks. CESM2-WACCM and UKESM1-0-LL are two of the only ESMs for which fully coupled SAI intervention experiments have been conducted. The remaining models, namely BCC-CSM2-MR, CESM2, CMCC-CM2-SR5, CMCC-ESM2, GFDL-ESM4, IPSL-CM6A-LR, and MRI-ESM2-0, are widely used, well-validated CMIP6 models that together provide a diverse set of dynamical cores and physical parameterizations, increasing robustness to structural uncertainty. Importantly, each of these models provides simulations for historical and standard SSP scenarios (1-2.6/2-4.5/3-7.0/5-8.5) as well as multiple ensemble members. This collection therefore spans a representative cross-section of CMIP6 modeling centers while supporting both standard climate scenarios and specialized SAI experiments.

We ensure broad coverage of standard climate trajectories and intervention scenarios (Table S3). We include historical simulations and four SSP scenarios spanning strong mitigation (SSP1-2.6), moderate emissions (SSP2-4.5), regional-rivalry-driven warming (SSP3-7.0), and high-emissions futures (SSP5-8.5). These scenarios

Dataset	Climate	Model	Model $\times$ Scenarios	Intervention Scenarios	Simulation	Resolution	
	Models	$\times$ Scenarios	$\times$ Members	$\times$ Members	Years	Spatial	Temporal
ClimateBench [54]	1	5	11	0	1,183	$192 \times 288$	Monthly
ACE [56]	1	1	1	0	110	$180 \times 360$	6-Hourly
ClimateSet [25]	21	104	108	0	10,672	$192 \times 288$	Daily
ERA5 [19]	1	1	1	0	85	$720 \times 1440$	Hourly
ClimateSuite (Ours)	10	66	345	69	33,739	$192 \times 288$	Monthly

Table S1. Comparison of ClimateSuite to existing climate-scale datasets.

Climate Model	Historical / SSP	SAI	Years
BCC-CSM2-MR	5	0	839
CESM2	5	0	2847
CESM2-WACCM	5	15	3522
CMCC-CM2-SR5	5	0	2159
CMCC-ESM2	5	0	509
GFDL-ESM4	5	0	1011
IPSL-CM6A-LR	5	0	8455
MRI-ESM2-0	5	0	4216
NorESM2-LM	5	0	2294
UKESM1-0-LL	5	1	7887
<b>Total</b>	<b>50</b>	<b>16</b>	<b>33,739</b>

Table S2. Climate model and scenario breakdown in ClimateSuite.

collectively capture a range of plausible 21st-century forcing pathways used in CMIP6 and provide diverse data for training and evaluating models under a variety radiative environments. To study climate responses under SAI, we further incorporate historical and baseline control runs in addition to a variety of single-point, two-point, and multi-latitude injection strategies. These experiments span equatorial to high-latitude injections, fixed-mass versus controller-based deployment algorithms, and temperature targets ranging from  $0.5^\circ\text{C}$  to  $1.5^\circ\text{C}$  above pre-industrial levels. By grounding all intervention runs in a common SSP2-4.5 forcing scenario, we isolate the effect of aerosol injection while maintaining comparability across experimental designs. Together, this collection is a representative and scientifically comprehensive set of forcings that enables evaluation of models across conventional, extreme, and policy-relevant climate futures.

## C.2. Simulation Downloading

We acquire all datasets using publicly accessible portals and tools. We download external forcings from input4MIPs through the ESGF portal, ensuring consistency with the forcing datasets used in the original modeling center runs. For the standard CMIP6 historical and SSP simulations, we use ESMValCore [1] and acccmip6 [18] to automate search,

download, and integrity checks across ten models. We use both tools to increase coverage because each exposes a partially overlapping subset of CMIP6 replica servers. For the SAI experiments, we retrieve simulations via Globus. We obtain the UKESM1-0-LL SAI outputs directly from the Met Office ARISE portal [37].

## C.3. Data Processing

We process all data to standardized NetCDFs to provide an ML-friendly format while still facilitating common climate analysis. To standardize the spatial resolution among all climate models, we regrid with bilinear interpolation and enforce longitudinal periodicity, preserving large-scale spatial patterns to ensure physically smooth transitions between adjacent grid cells.

## D. Evaluation Metrics

### D.1. Preliminaries

Let  $\mathbf{X} \in \mathbb{R}^{E \times I \times J}$  denote an ensemble of predictions (i.e. multiple samples from different starting noise, all using the same conditioning), and  $\mathbf{Y} \in \mathbb{R}^{I \times J}$  the corresponding simulation targets, where  $E$  is the number of ensemble members,  $I$  the number of latitudes, and  $J$  the number of longitudes in the grid. Let  $\bar{\mathbf{X}} = \frac{1}{E} \sum_{e=1}^E$  be the prediction averaged over ensemble members. Define  $w(i)$  to be the normalized latitude-dependent area weight at latitude  $i$ , such that

$$\frac{1}{I} \sum_{i=1}^I w(i) = 1,$$

These weights account for the decreasing surface area of grid cells toward the poles. They are therefore used to compute spatially unbiased means and evaluation metrics, a standard practice in weather and climate prediction [5, 38, 44, 54].

### D.2. Metric definitions

We report the area-weighted average Root Mean Square Error (RMSE) and Bias of the member-averaged predictions



Scenario	Description
historical	Standard historical simulation from 1850 to near-present using observed forcings
ssp126	Future scenario under SSP1-2.6, representing strong mitigation and low greenhouse-gas forcing
ssp245	Future scenario under SSP2-4.5, a middle-of-the-road pathway of moderate emissions
ssp370	Future scenario under SSP3-7.0 representing regional rivalry and higher forcing
ssp585	Future scenario under SSP5-8.5, representing high emissions and fossil-fuel driven development
MA-HISTORICAL	Historical baseline simulation (pre-intervention control run)
MA-BASELINE	Baseline simulation without any intervention or injection applied, under future forcing
SINGLE-POINT-INJANN0N_12Tg	Single-point injection at 0°N (equator), 12 Tg total
SINGLE-POINT-INJANN15S_12Tg	Single-point injection at 15°S, 12 Tg total
SINGLE-POINT-INJANN15N_12Tg	Single-point injection at 15°N, 12 Tg total
SINGLE-POINT-INJANN30N_12Tg	Single-point injection at 30°N, 12 Tg total
SINGLE-POINT-INJANN30S_12Tg	Single-point injection at 30°S, 12 Tg total
SINGLE-POINT-INJMAM60N_12Tg	Single-point injection at 60°N, 12 Tg total
SINGLE-POINT-INJSON60S_12Tg	Single-point injection at 60°S, 12 Tg total
SSP245-MA-GAUSS-DEFAULT	Injection with a controller-based algorithm at 15°S, 15°N, 30°S, 30°N to maintain temperature near 1.5°C above pre-industrial (PI) levels
SSP245-MA-GAUSS-LOWER-0.5	Injection with a controller-based algorithm targeting 0.5°C above PI
SSP245-MA-GAUSS-LOWER-1.0	Injection with a controller-based algorithm targeting 1.0°C above PI
SSP245-MA-GAUSS15N_15S-LOWER-0.5	Two-point injection at ±15°N/S targeting 0.5°C above PI
SSP245-MA-GAUSS30N_30S-LOWER-0.5	Two-point injection at ±30°N/S targeting 0.5°C above PI
SSP245-MA-GAUSS0N-LOWER-0.5	Single-point injection at 0°N targeting 0.5°C above PI
SAI-1.5	Multi-latitude injection targeting 1.5°C above PI

Table S3. **Standard emissions and intervention scenarios included in ClimateSuite.** Both historical simulations use CESM2-WACCM and all non-historical SAI simulations use CESM2-WACCM and SSP2-4.5 as the base forcing scenario, except for SAI-1.5 which uses UKESM1-0-LL (under SSP2-4.5).

compared to the targets as follows:

$$\text{Bias} = \frac{1}{IJ} \sum_{i,j} w(i) (\bar{\mathbf{X}}_{i,j} - \mathbf{Y}_{i,j}), \quad (16)$$

$$\text{RMSE} = \sqrt{\frac{1}{IJ} \sum_{i,j} w(i) (\bar{\mathbf{X}}_{i,j} - \mathbf{Y}_{i,j})^2}. \quad (17)$$

Values closer to zero are better for Bias and lower values are better for RMSE.

We additionally evaluate the full ensemble forecast using the unbiased version of the CRPS [36]:

$$\text{CRPS} = \frac{1}{IJ} \sum_{i,j} w(i) \left[ \frac{1}{E} \sum_{e=1}^E |\mathbf{X}_{e,i,j} - \mathbf{Y}_{i,j}| - \frac{1}{2E(E-1)} \sum_{e=1}^E \sum_{f=1}^E |\mathbf{X}_{e,i,j} - \mathbf{X}_{f,i,j}| \right]. \quad (18)$$

The first term represents the accuracy (or skill) of the ensemble, while the second term quantifies its internal spread. The conventional, biased form of CRPS averages the spread using a factor of  $\frac{1}{2E^2}$ , which introduces bias for small ensembles. The unbiased formulation instead employs  $\frac{1}{2E(E-1)}$ , providing a more reliable measure of ensemble performance. Lower CRPS values indicate better forecasts. For deterministic models ( $E = 1$ ),  $\bar{\mathbf{X}}_{i,j} = \mathbf{X}_{i,j}$  and CRPS simplifies to the mean absolute error (MAE).

## E. Additional Results

### E.1. Long Sequence Runtimes

A major benefit of SPF’s design is the capability of caching intermediate states to save computation for long sequences. We show this visually for a dummy example in Figure S1. To demonstrate this empirically, we report the runtimes for generating a 100-year sequence at both the yearly and monthly timescales (Table S4). Efficiency gains compared

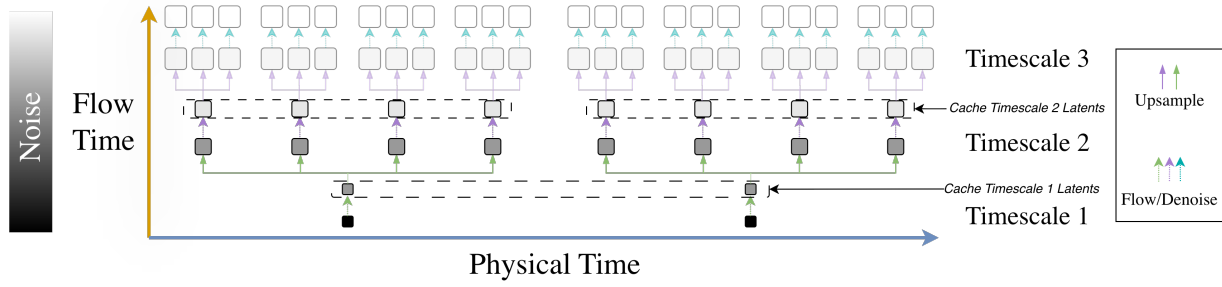


Figure S1. **Efficiency benefits from caching.** For long sequence generation, intermediate latents at coarser timescales can be cached to save compute when generating samples from finer timescales. In this dummy example, to generate a sequence of eight fine timescale samples, the flow in Timescale 1 only needs to be run once and the flow in Timescale 2 only needs to be run twice. Then, only the last part of the flow in Timescale 3 needs to be run when generating each of the eight clean Timescale 3 samples as the flow can resume from the Timescale 2 latents.

Model	Native Timescale	Yearly Runtime (s)	Monthly Runtime (s)
<i>100M Parameters</i>			
ClimaX Frozen [38]	Yearly	2	-
UNet [45]	Yearly	1	-
ClimaX [38]	Yearly	2	-
Pyramidal Flow [24]	Yearly	190	-
Multi-Yearly Flow (Ours)	Yearly	20	-
Multi-Monthly Flow (Ours)	Monthly	112	112
Pyramidal Flow [24]	Monthly	844	844
PixelFlow [8]	Yearly	60	-
SPF (Ours)	Multi	21	52
<i>200M Parameters</i>			
UNet [45]	Yearly	9	-
Pyramidal Flow [24]	Yearly	239	-
Multi-Yearly Flow (Ours)	Yearly	41	-
Pyramidal Flow [24]	Monthly	1054	1054
Multi-Monthly Flow (Ours)	Monthly	213	213
PixelFlow [8]	Yearly	71	-
SPF (Ours)	Multi	42	100

Table S4. **Per-timescale runtime for a single 100 year sample.**

to the other models are further emphasized in this long sequence setting, with SPF achieving much faster results than all probabilistic models on both timescales except for Multi-Yearly flow at the yearly timescale, for which it nearly matches in runtime. Importantly, SPF can generate 100-year probabilistic samples of monthly data in 1-2 minutes, which is much faster than previous weather-scale autoregressive models (which take nearly 3 hours) and massively faster than the physical simulations (which take weeks to months).

## E.2. Other Results

We report a variety of additional results, including tuning ClimaX settings (Table S5), global means of SPF compared to simulations in ClimateBench (Figures S2–S3), SPF histograms on ClimateBench (Figures S4–S5), SPF samples on ClimateBench (Figures S6–S11), multi-model global means of SPF compared to simulations in ClimateSuite (Figures S12), SPF histograms on ClimateSuite (Fig-

Procedure	Resolution	Patch Size	RMSE
Fine-Tuned	High	16	0.546
Fine-Tuned	High	4	0.556
Fine-Tuned	Low	2	0.577
Fine-Tuned	Low	16	0.594
Frozen	High	16	0.619
Frozen	Low	16	0.721
Frozen	High	4	0.721
Frozen	Low	2	0.811

Table S5. **ClimateBench yearly temporal resolution results under different ClimaX variants.**

ures S13–S14), SPF samples of multiple models in ClimateSuite (Figures S15–S18), and an ablation measuring the impact of using variable number of ensemble members on SPF performance on ClimateBench (Figure S19).

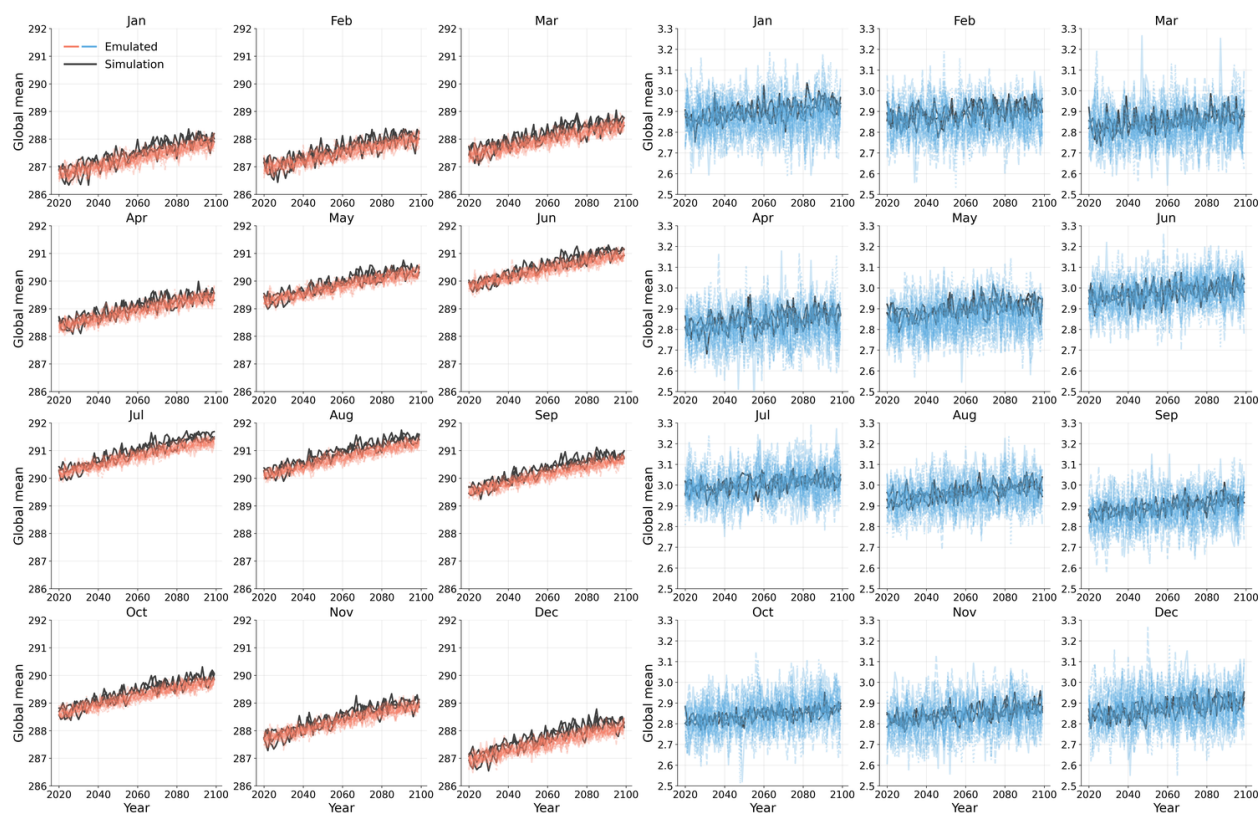


Figure S2. **Monthly latitude-weighted global means of the 200M SPF on ClimateBench SSP2-4.5.** Temperature shown in the left three columns (red) and precipitation in the right three columns (blue).

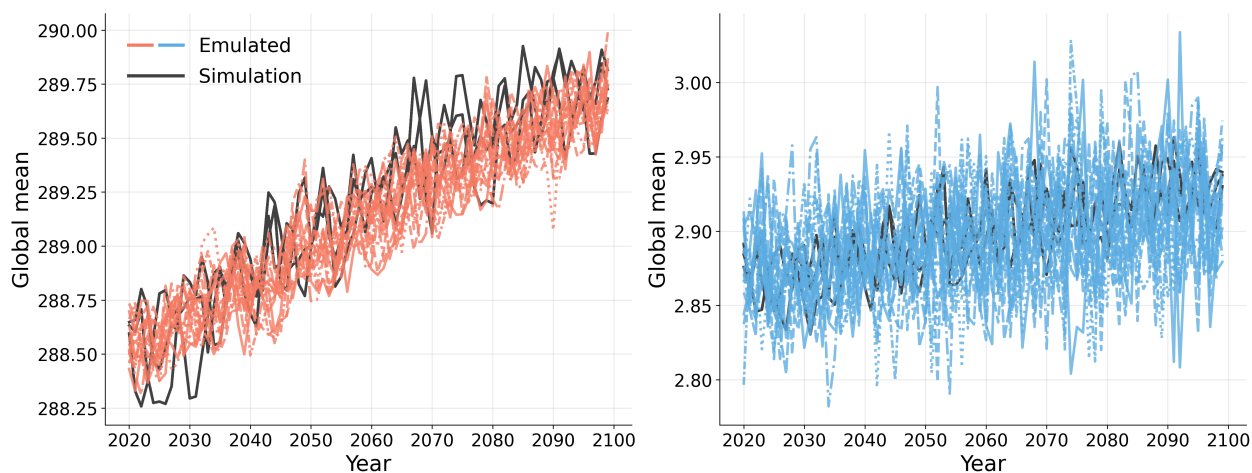


Figure S3. **Yearly latitude-weighted global means of the 200M SPF on ClimateBench SSP2-4.5.** Temperature shown in the left column (red) and precipitation in the right column (blue).

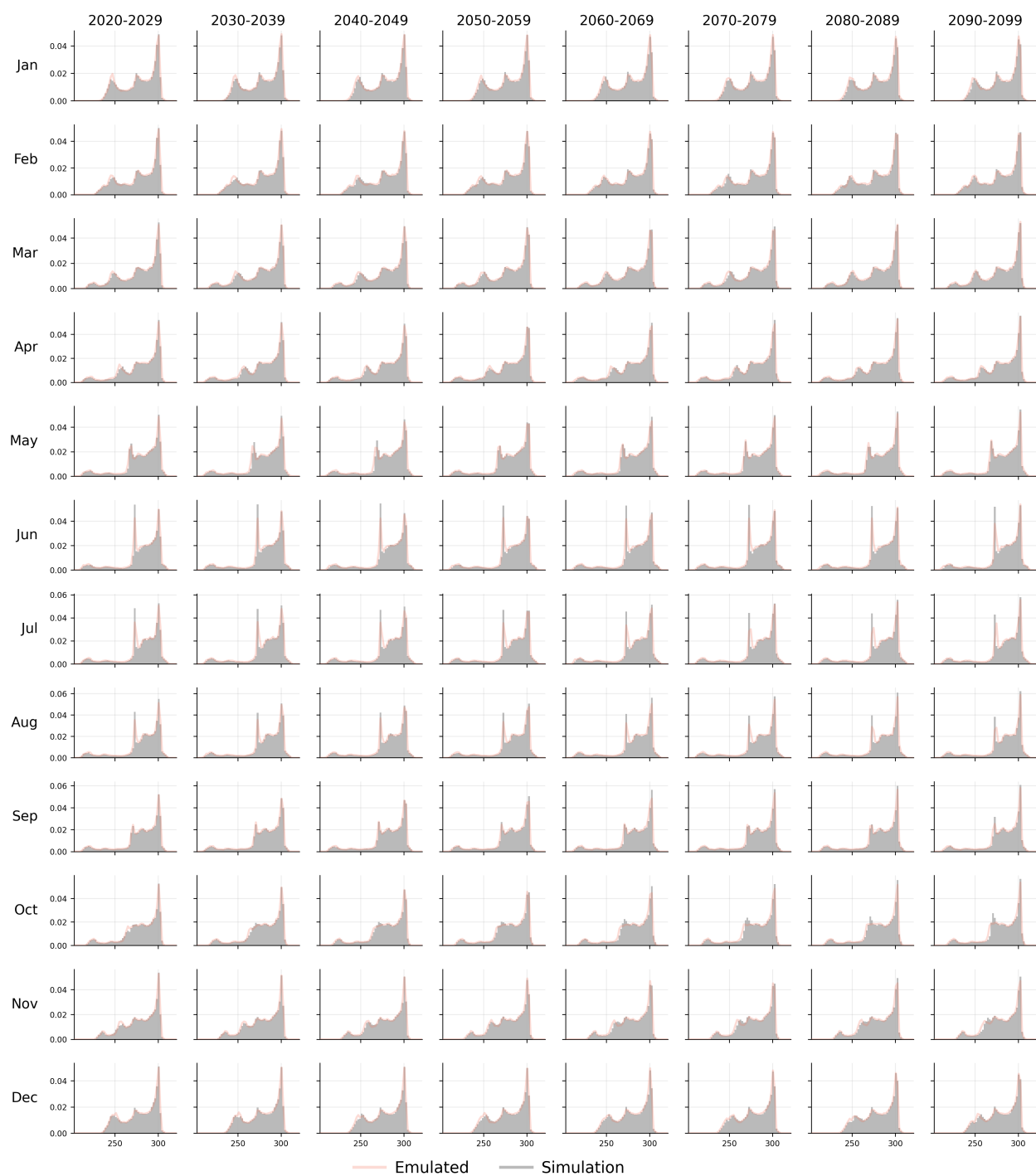


Figure S4. **Monthly temperature histograms of the 200M SPF model on ClimateBench SSP2-4.5, broken down by month and decade.**



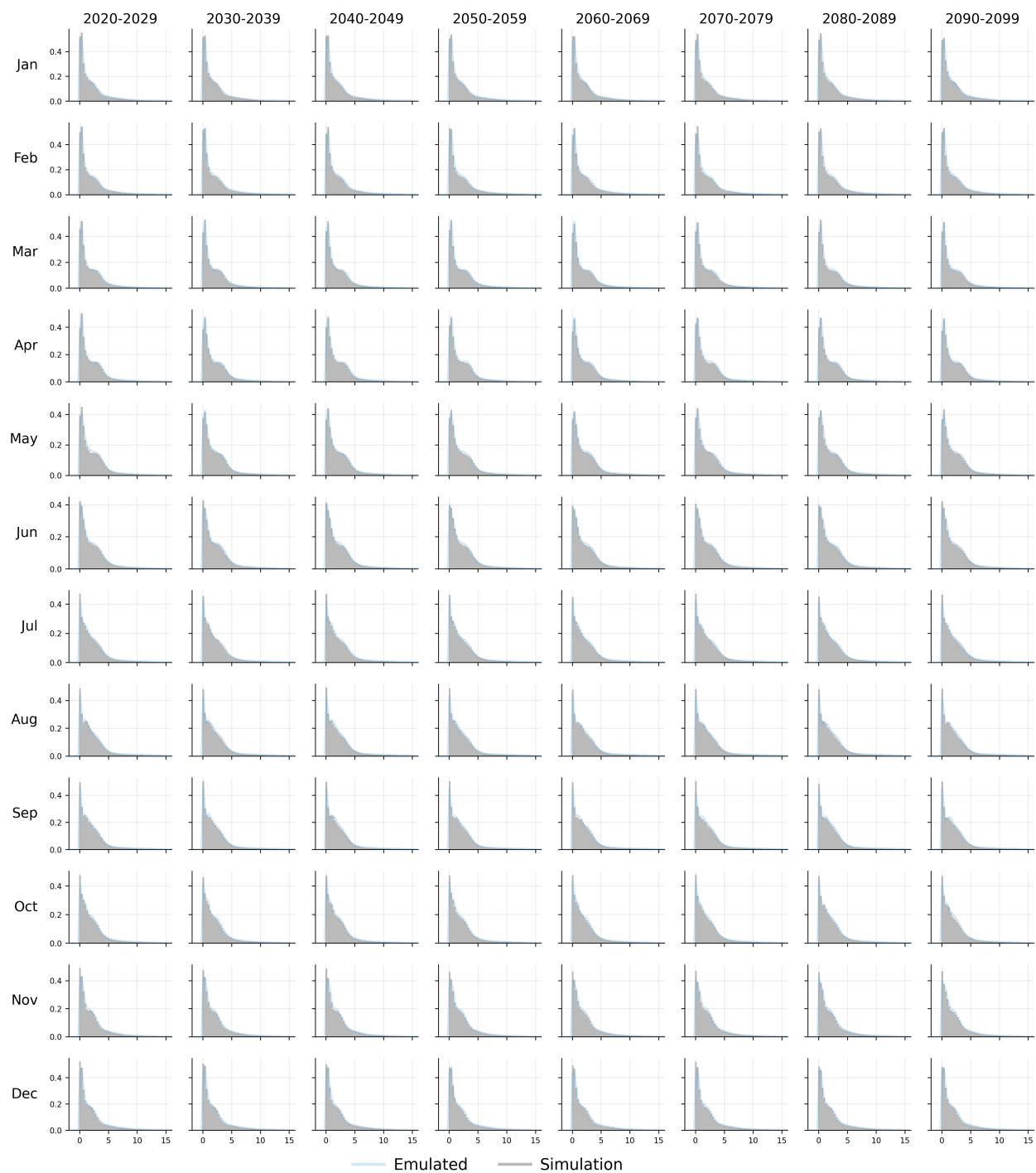


Figure S5. **Monthly precipitation histograms of the 200M SPF model on ClimateBench SSP2-4.5, broken down by month and decade.**

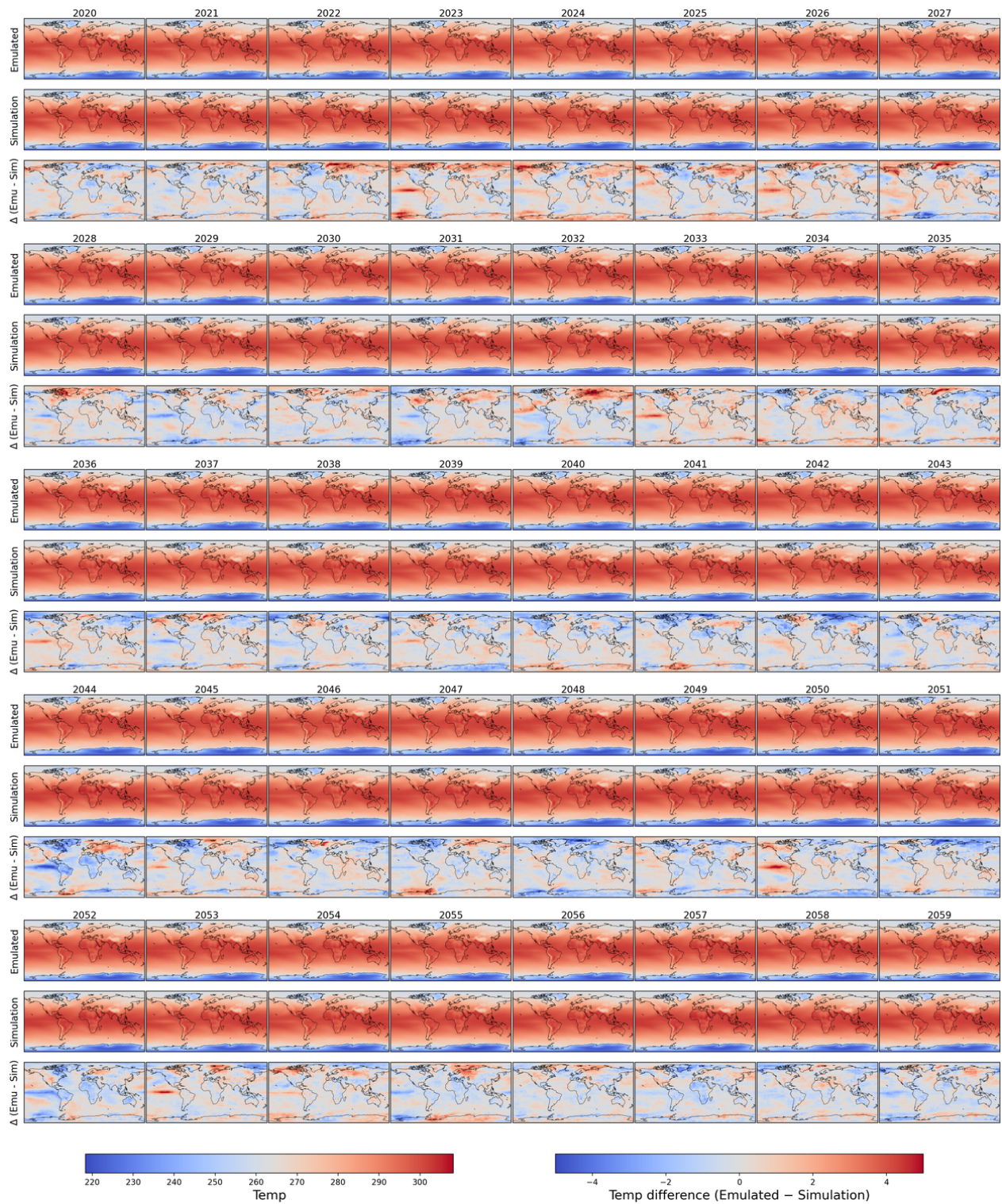


Figure S6. ClimateBench samples of yearly emulated, simulated, and difference temperature maps (2020–2059, SSP2-4.5).



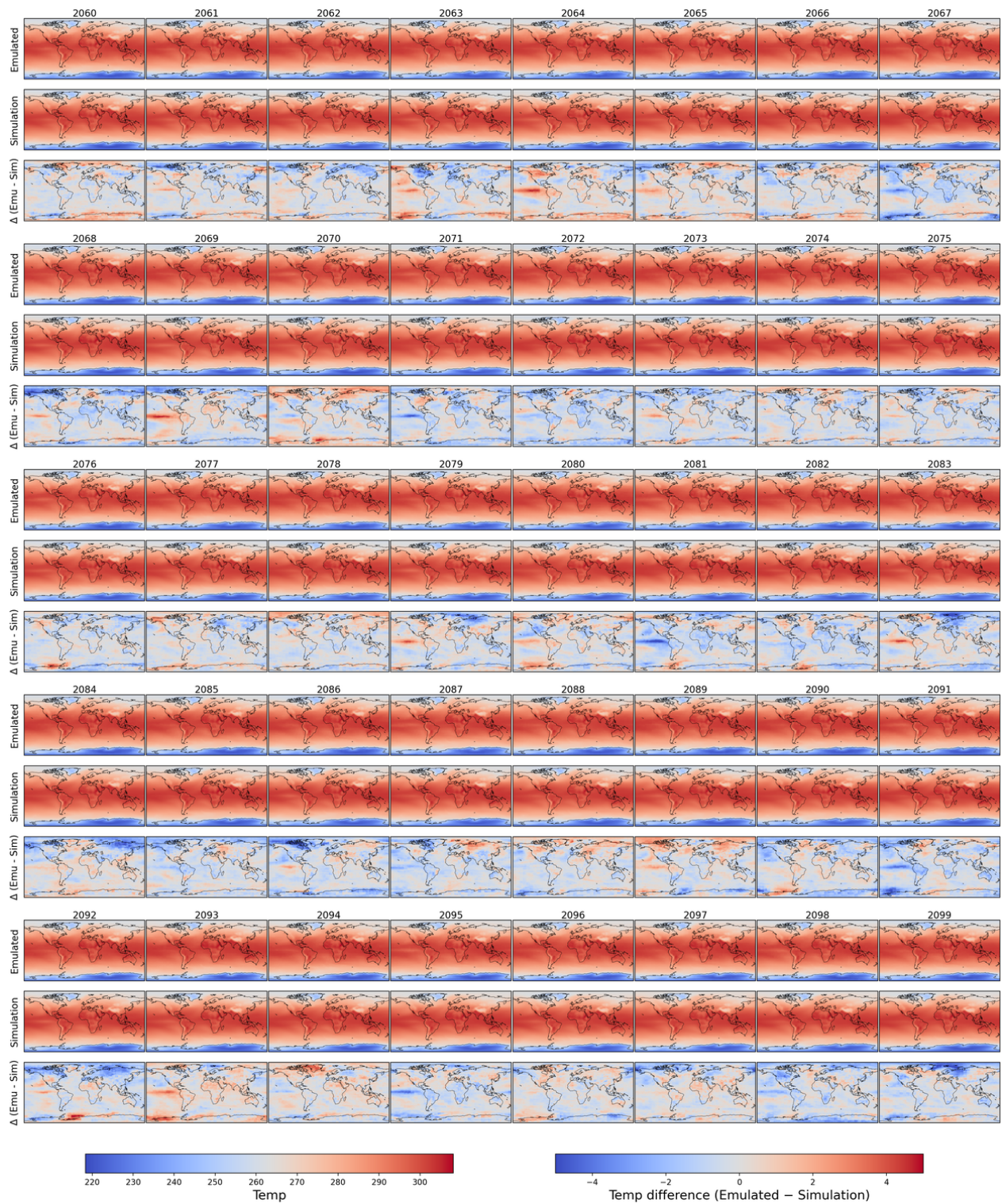


Figure S7. ClimateBench samples of yearly emulated, simulated, and difference temperature maps (2060–2099, SSP2-4.5).



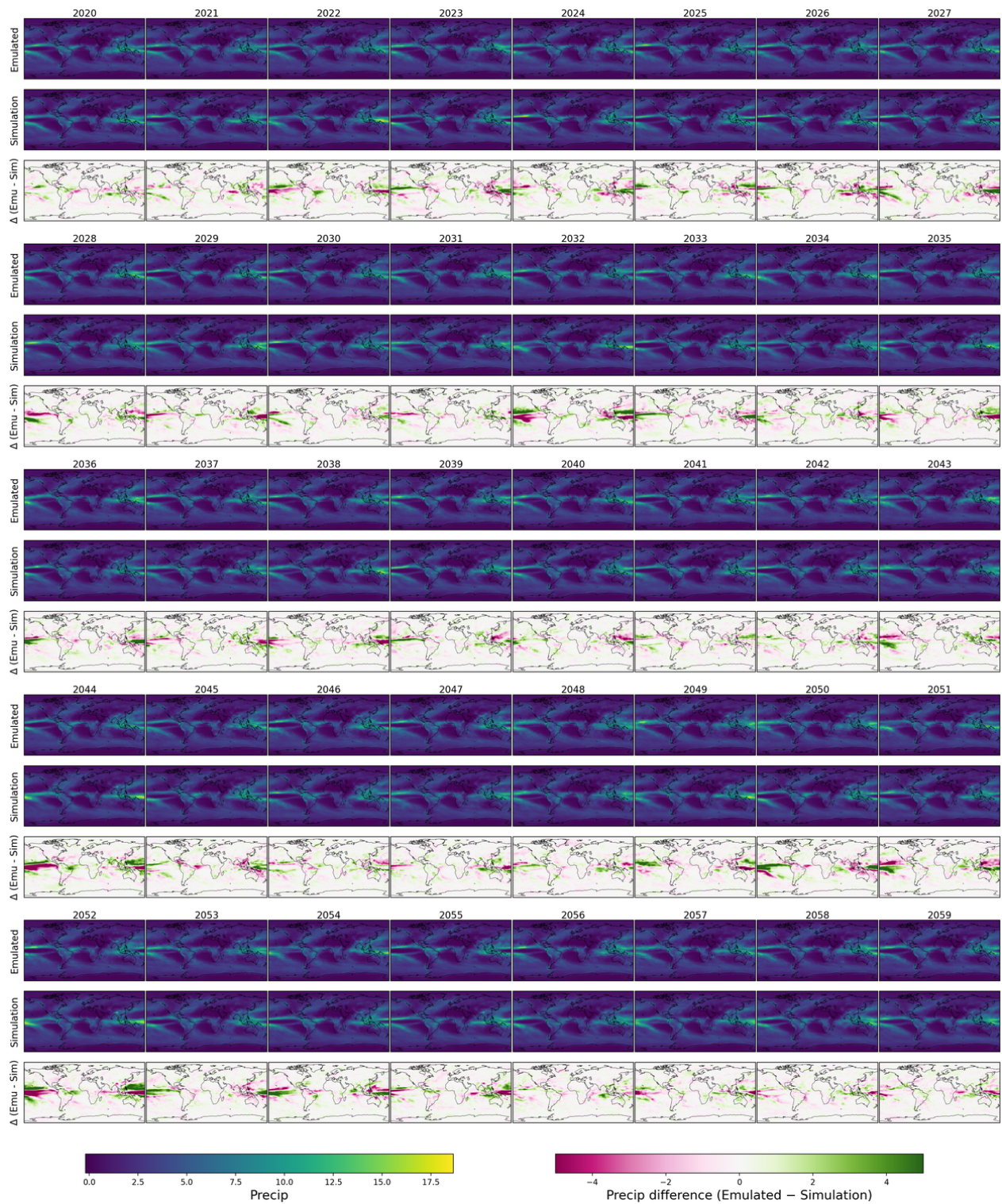


Figure S8. ClimateBench samples of yearly emulated, simulated, and difference precipitation maps (2020–2059, SSP2-4.5).



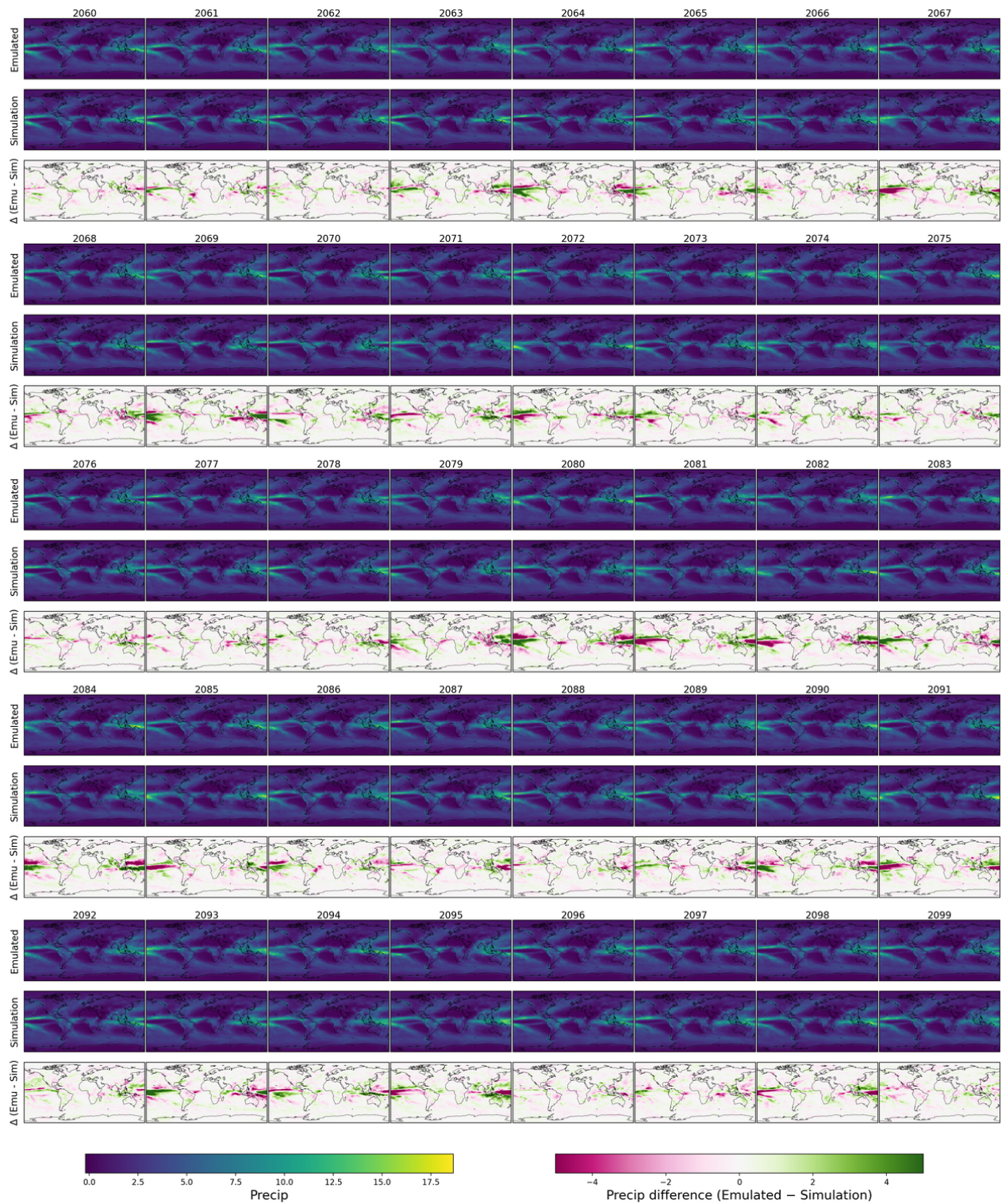


Figure S9. ClimateBench samples of yearly emulated, simulated, and difference precipitation maps (2060–2099, SSP2-4.5).



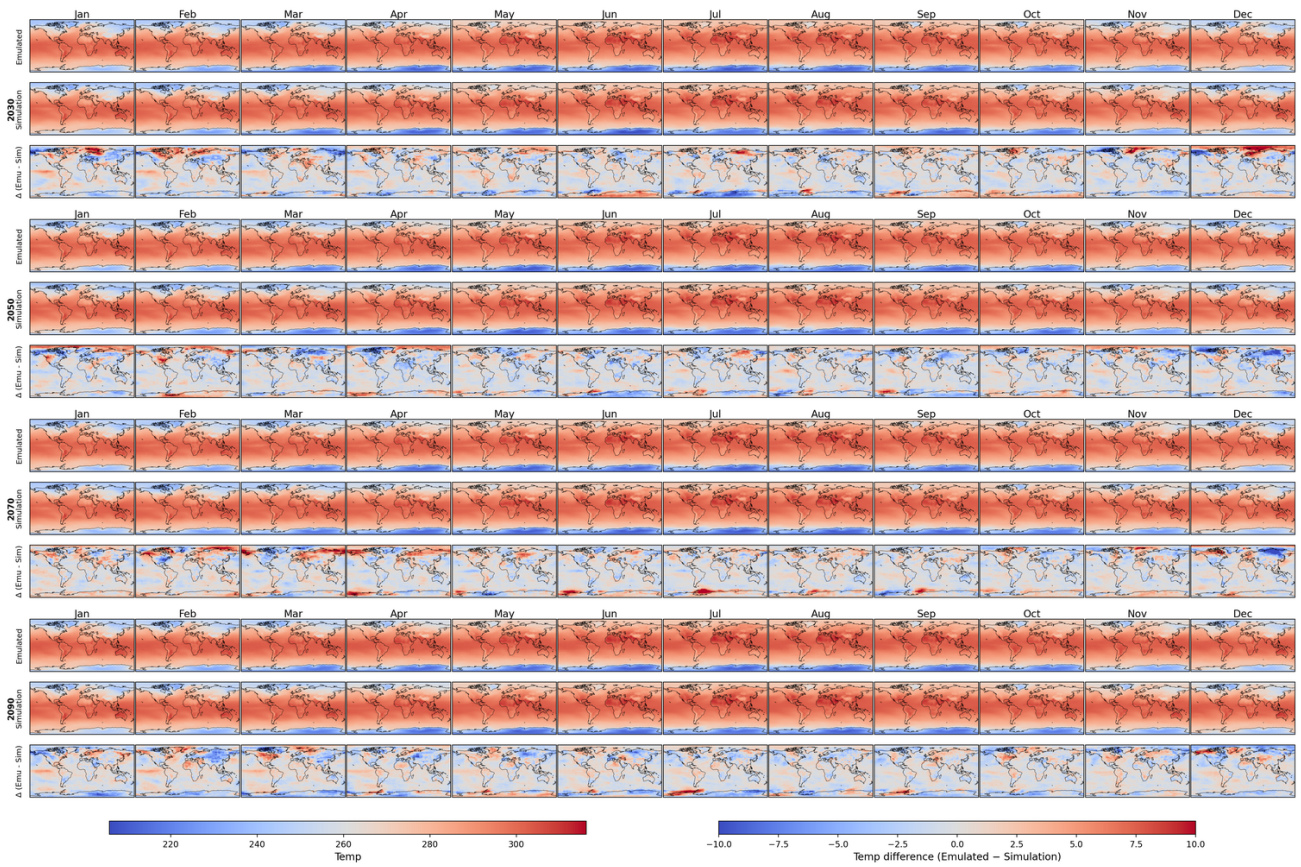


Figure S10. ClimateBench samples of monthly emulated, simulated, and difference temperature maps (SSP2-4.5).

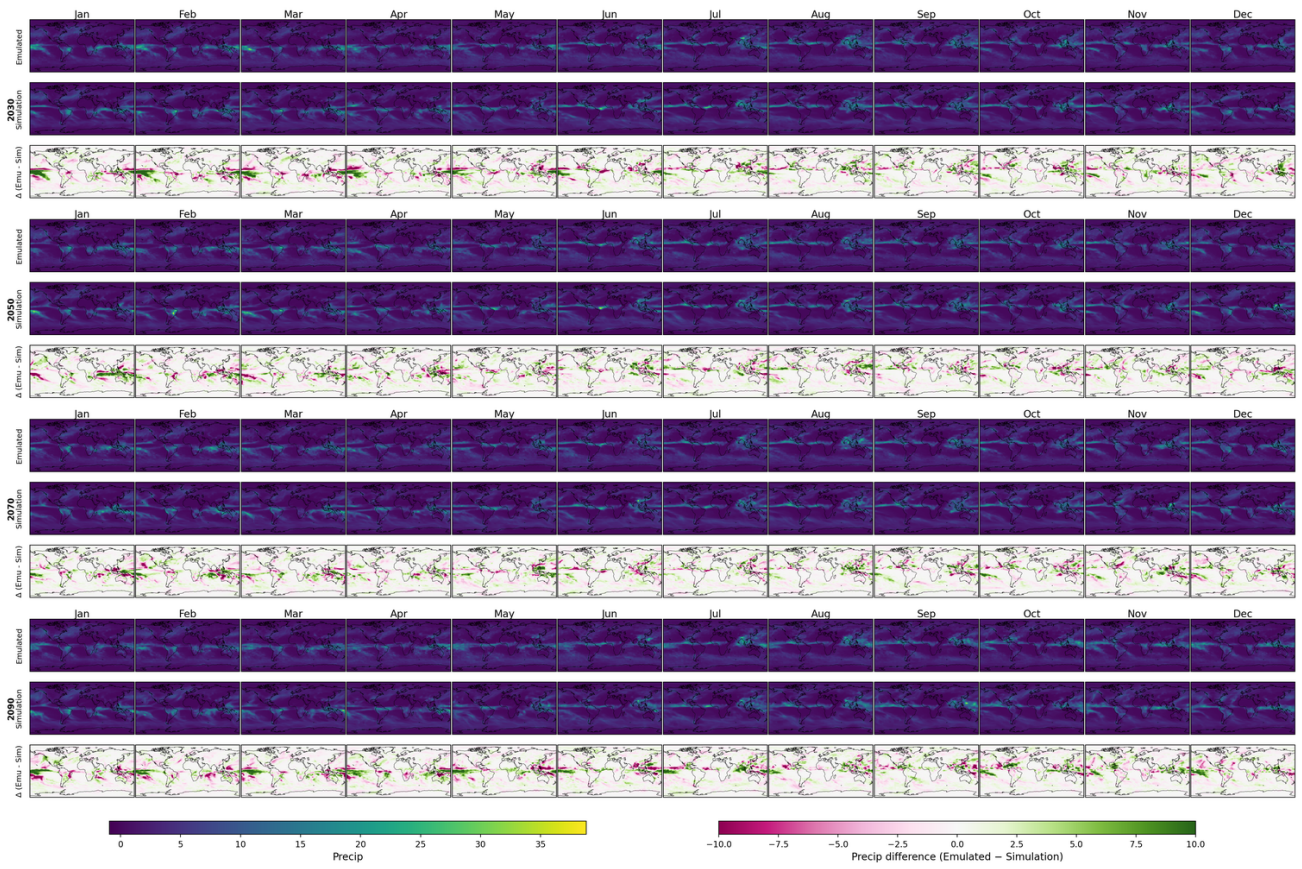


Figure S11. ClimateBench samples of monthly emulated, simulated, and difference precipitation maps (SSP2-4.5).

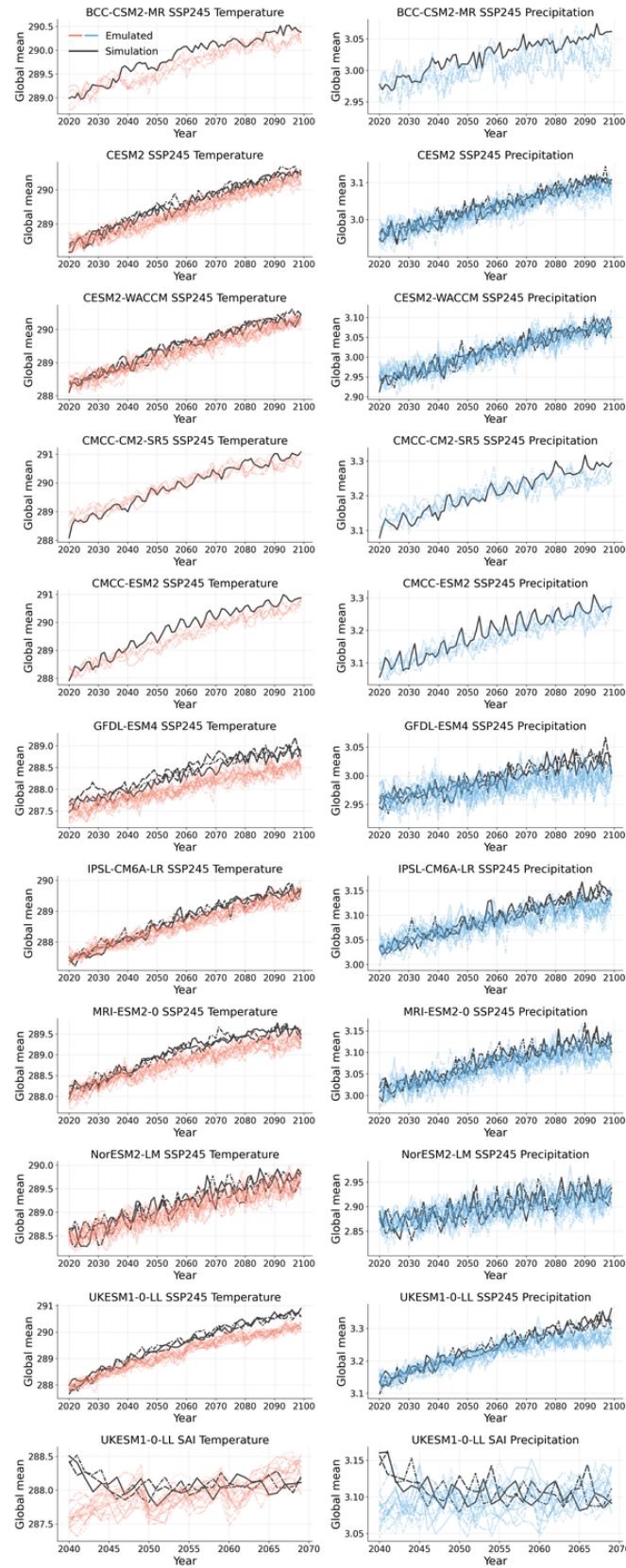


Figure S12. Yearly latitude-weighted global means of the 600M SPF model on SSP2-4.5 across the 10 climate models and the SAI experiment on UKESM1-0-LL in ClimateSuite.22



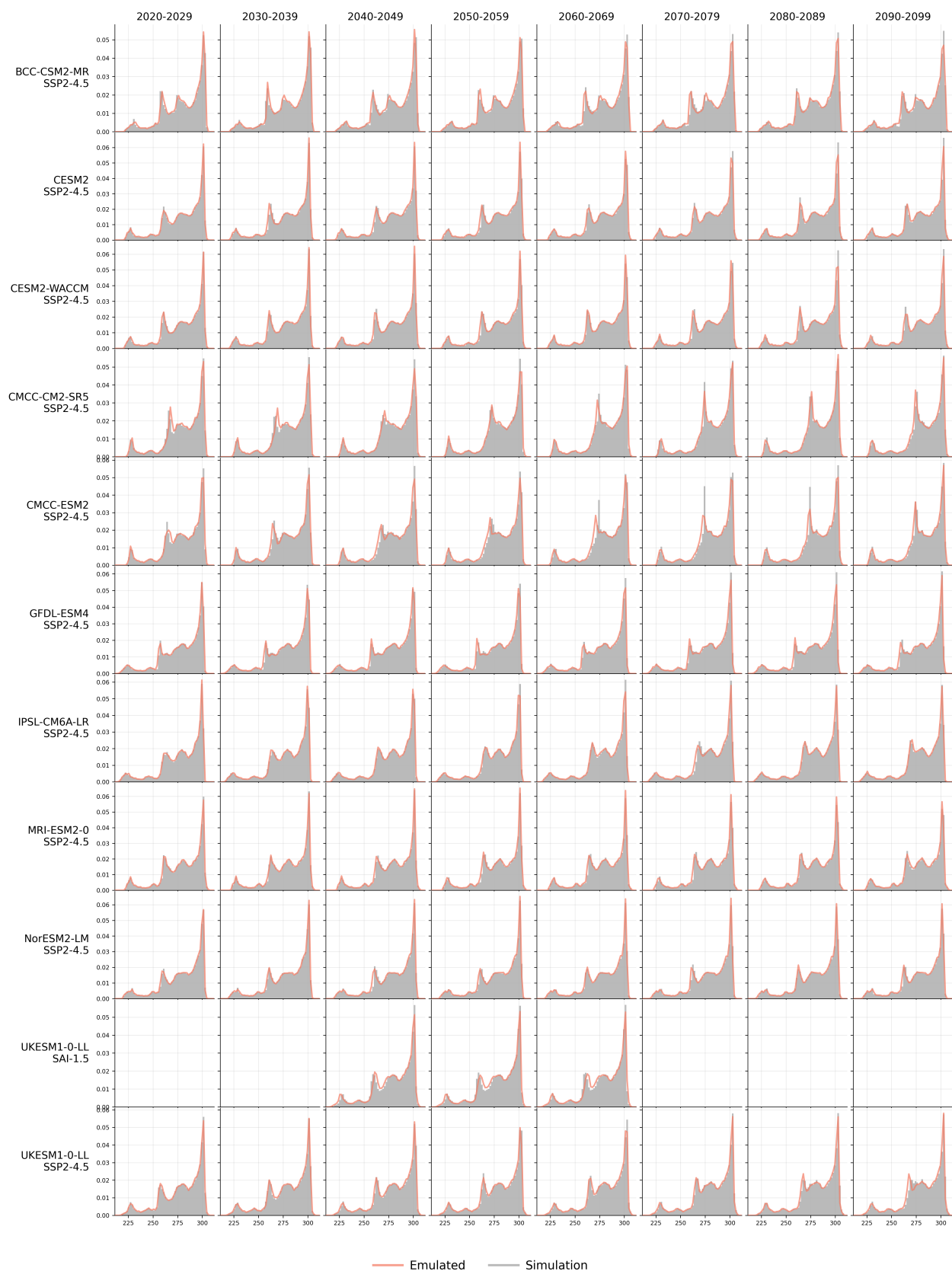
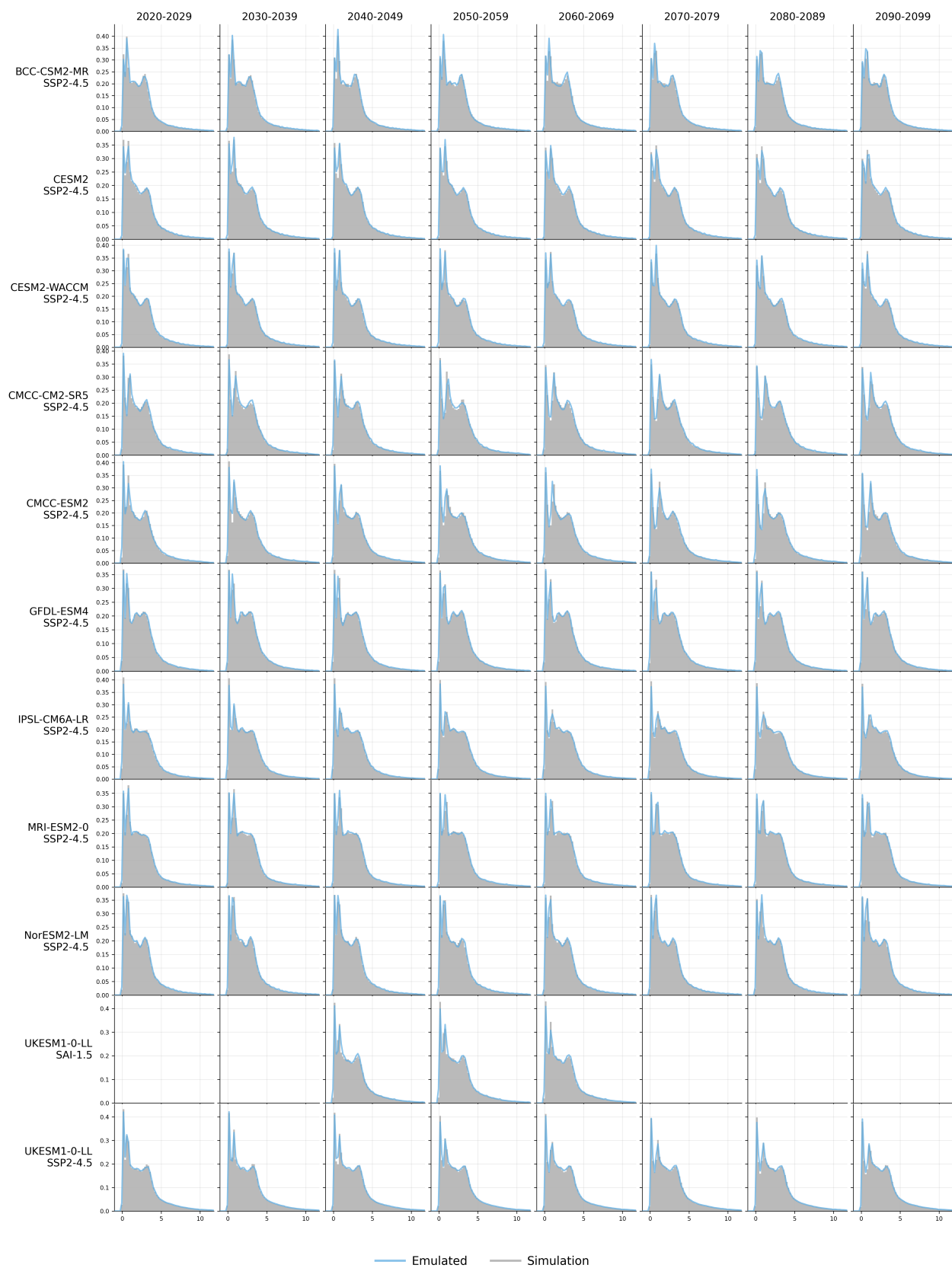


Figure S13. Yearly temperature histograms of the 600M SPF model on SSP2-4.5 across the 10 climate models and the SAI experiment on UKESM1-0-LL, broken down by decade.





**Figure S14. Yearly precipitation histograms of the 600M SPF model on SSP2-4.5 across the 10 climate models and the SAI experiment on UKESM1-0-LL, broken down by decade.**

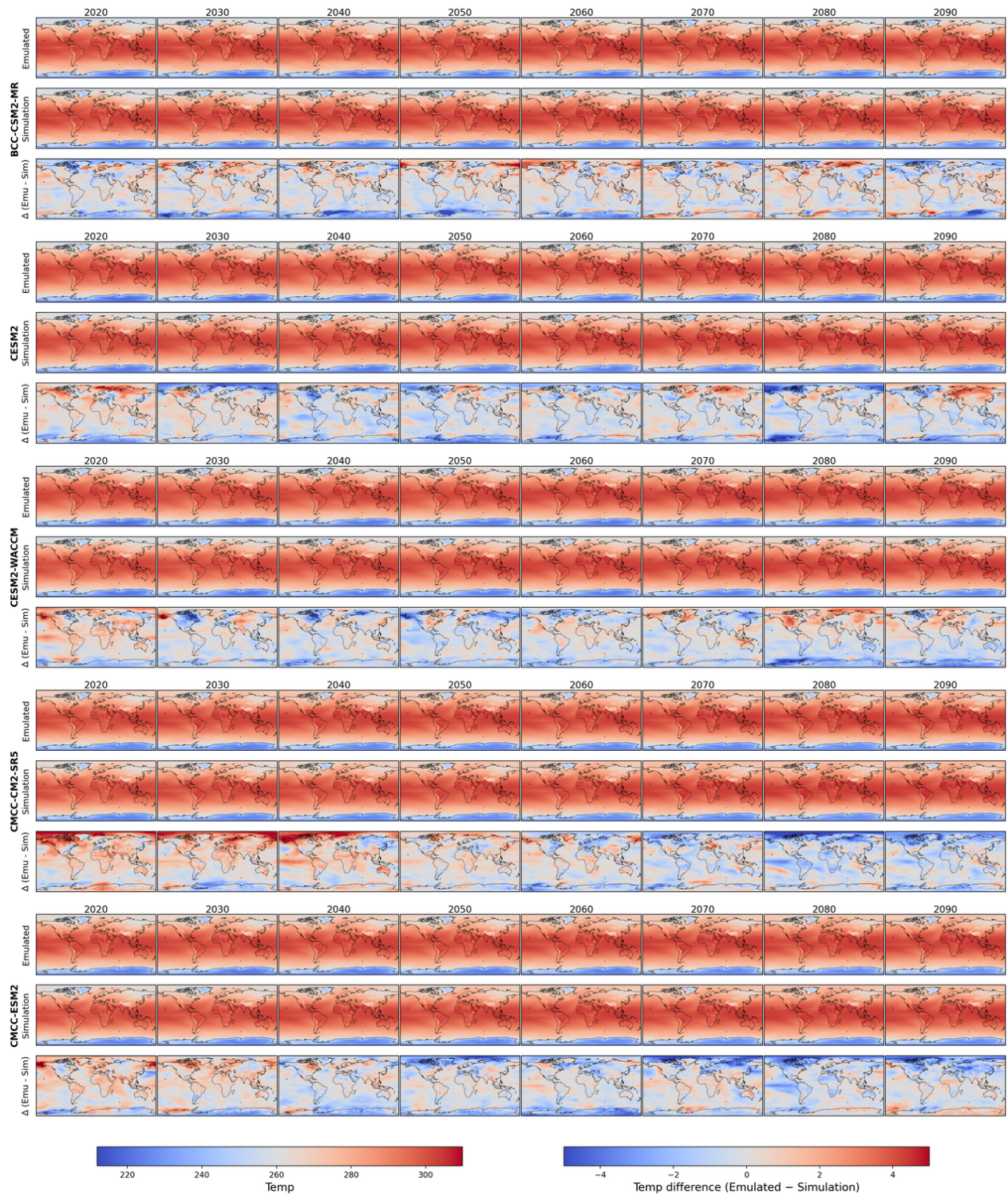


Figure S15. Per-model ClimateSuite samples of yearly emulated, simulated, and difference temperature maps (SSP2-4.5).



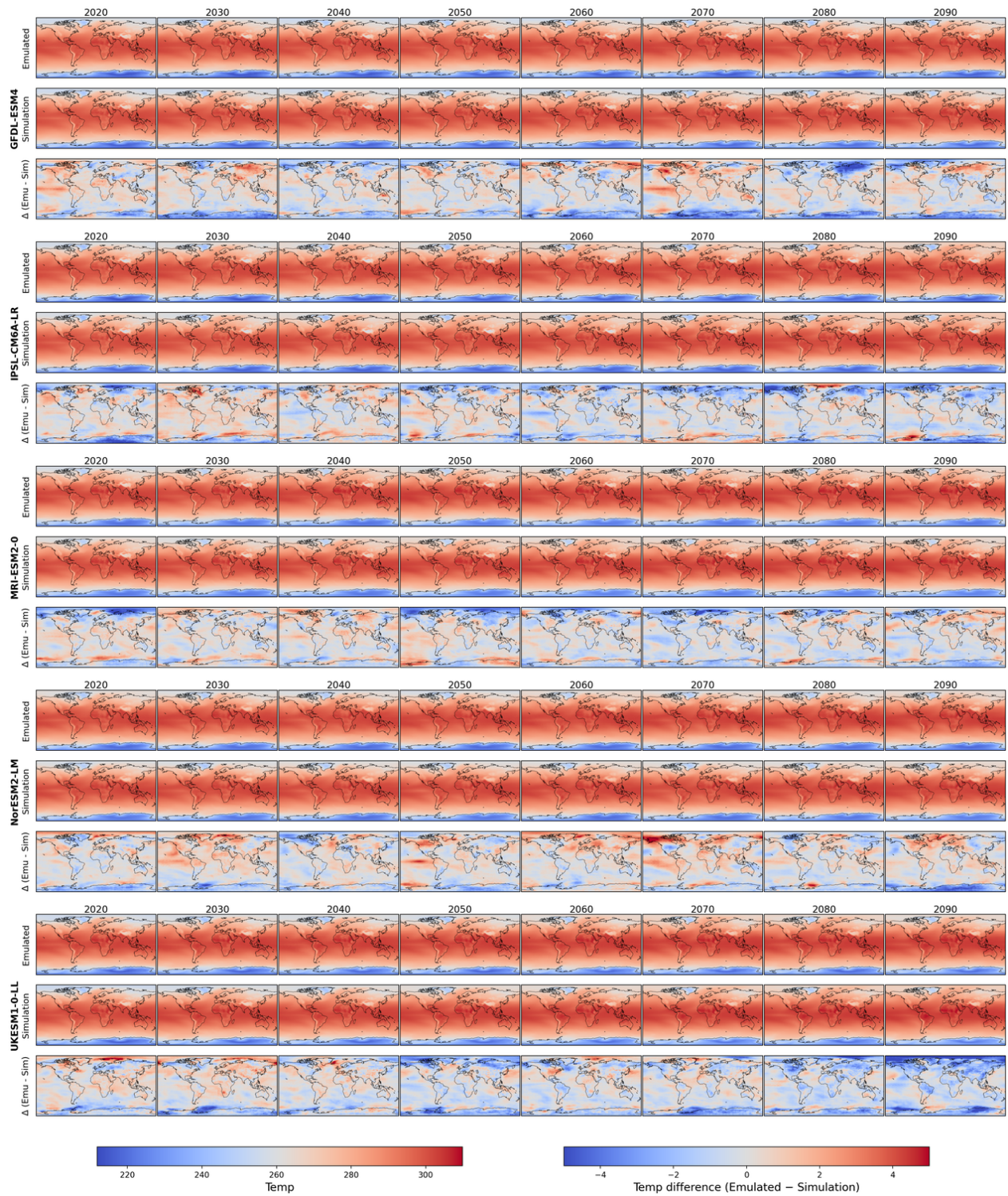


Figure S16. Per-model ClimateSuite samples of yearly emulated, simulated, and difference temperature maps (SSP2-4.5).



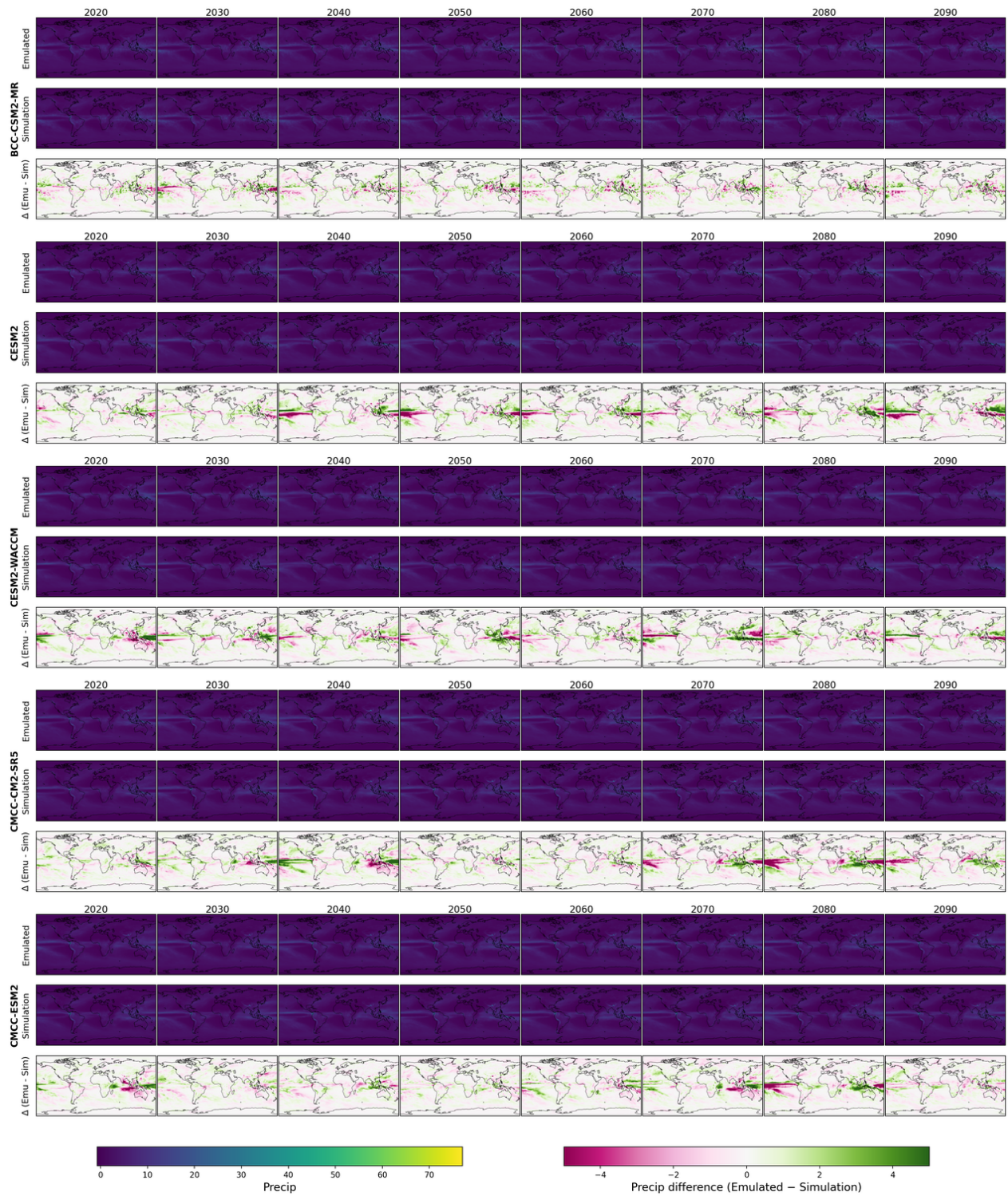


Figure S17. Per-model ClimateSuite samples of yearly emulated, simulated, and difference precipitation maps (SSP2-4.5).



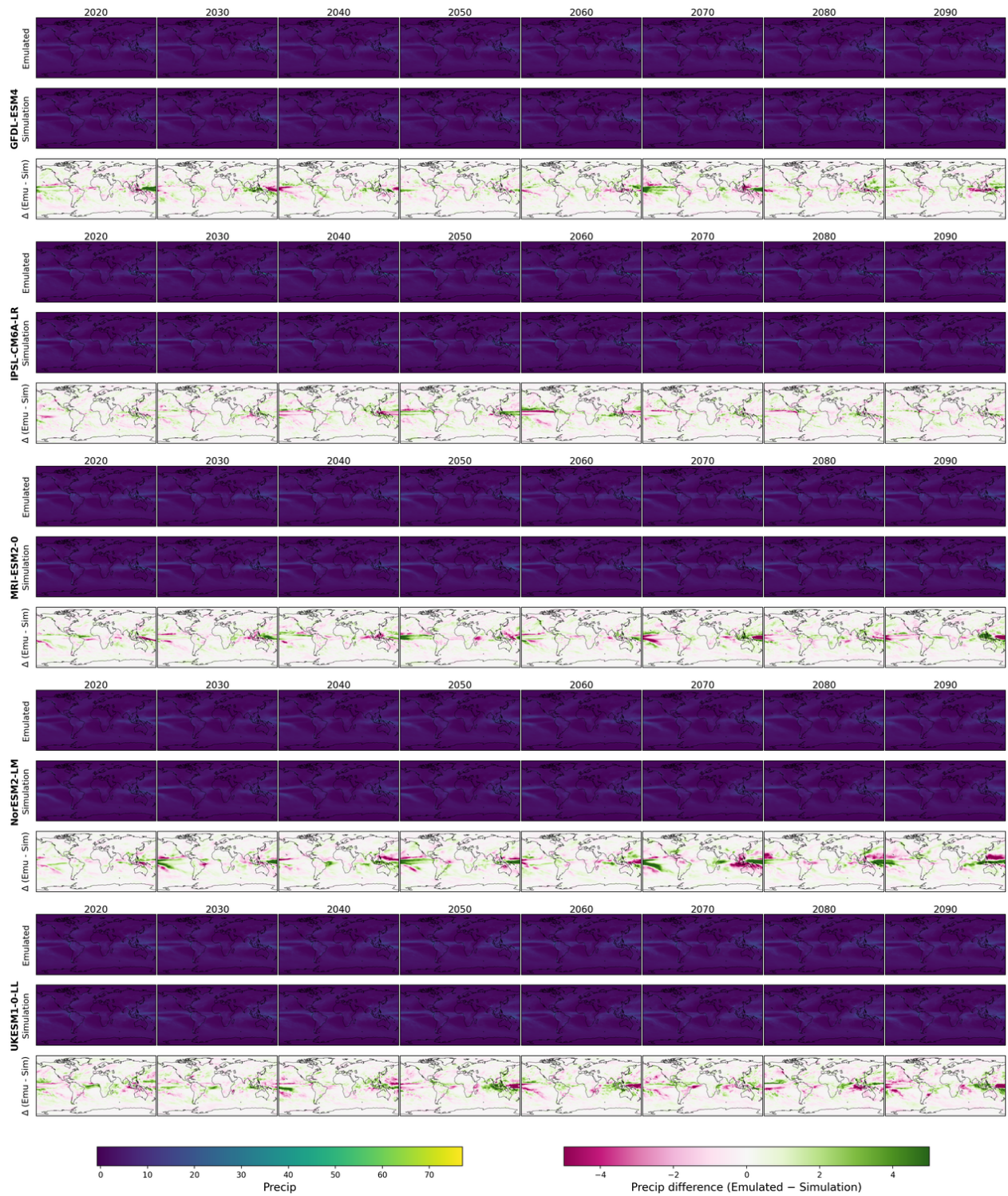


Figure S18. Per-model ClimateSuite samples of yearly emulated, simulated, and difference precipitation maps (SSP2-4.5).

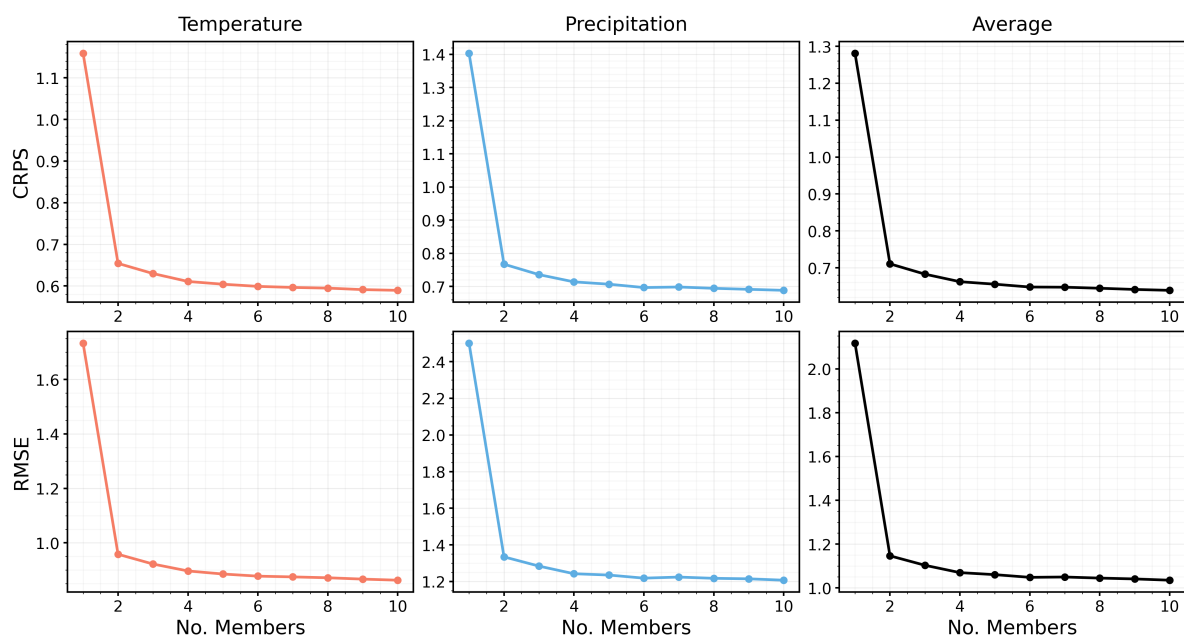


Figure S19. Effect of number of members on SPF performance on ClimateBench SSP2-4.5.